PDK4 dictates metabolic resistance to ferroptosis by suppressing pyruvate oxidation and fatty acid synthesis

Xinxin Song, Jiao Liu, Feimei Kuang, Xin Chen, Herbert J Zeh, Rui Kang, Guido Kroemer, Yangchun Xie, Daolin Tang

Cell Reports

Article

PDK4 dictates metabolic resistance to ferroptosis by suppressing pyruvate oxidation and fatty acid synthesis

Graphical Abstract

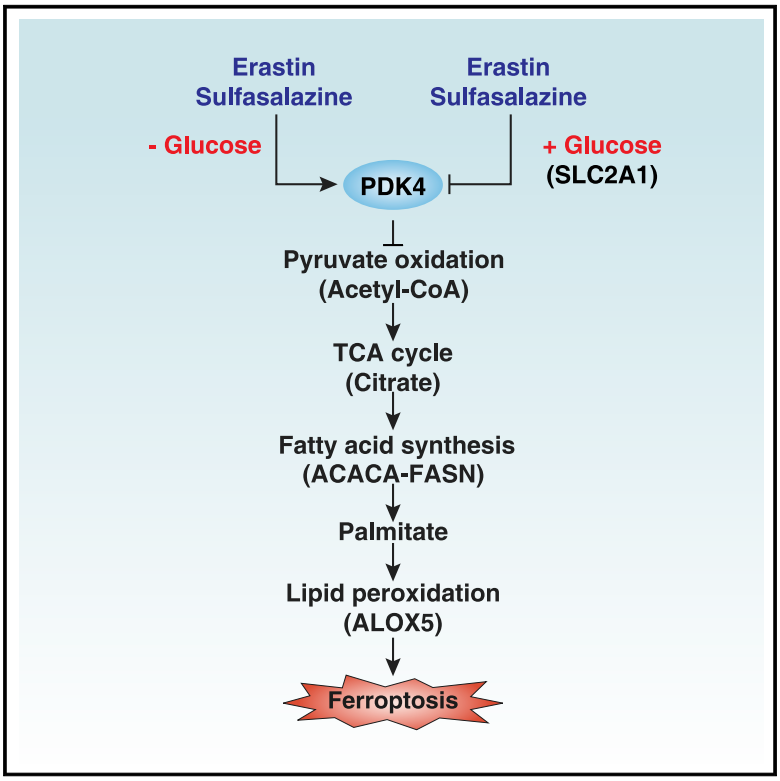

Highlights

- SLC2A1-dependent glucose uptake facilitates ferroptosis
- Pyruvate oxidation-dependent fatty acid synthesis facilitates ferroptosis
- PDK4 is a key metabolic regulator of ferroptosis resistance
- High-fat diet promotes ferroptotic cell death *in vivo*

Authors

Xinxin Song, Jiao Liu, Feimei Kuang, ..., Guido Kroemer, Yangchun Xie, Daolin Tang

Correspondence

xieyangchun88@csu.edu.cn (Y.X.), daolin.tang@utsouthwestern.edu (D.T.)

In brief

Song et al. demonstrate that PDK4 plays a role in preventing ferroptosis by inhibiting pyruvate oxidation and subsequent fatty acid synthesis and lipid peroxidation in pancreatic cancer cells. These findings indicate that targeting glucose metabolic pathways has the potential to modulate ferroptosis sensitivity in cancer therapy.

Song et al., 2021, Cell Reports *34*, 108767
February 23, 2021
https://doi.org/10.1016/j.celrep.2021.108767

CellPress

Cell Reports

CellPress
OPEN ACCESS

Article

PDK4 dictates metabolic resistance to ferroptosis by suppressing pyruvate oxidation and fatty acid synthesis

Xinxin Song,[1,11] Jiao Liu,[2,11] Feimei Kuang,[2] Xin Chen,[1] Herbert J. Zeh III,[1] Rui Kang,[1] Guido Kroemer,[3,4,5,6,7,8,9] Yangchun Xie,[10,*] and Daolin Tang[1,12,*]

[1]Department of Surgery, UT Southwestern Medical Center, Dallas, TX, USA
[2]The Third Affiliated Hospital, Guangzhou Medical University, Guangdong, China
[3]Université Paris Descartes, Sorbonne Paris Cité, 75006 Paris, France
[4]Equipe 11 labellisée Ligue Nationale contre le Cancer, Centre de Recherche des Cordeliers, 75006 Paris, France
[5]Institut National de la Santé et de la Recherche Médicale, U1138, Paris, France
[6]Université Pierre et Marie Curie, 75006 Paris, France
[7]Metabolomics and Cell Biology Platforms, Gustave Roussy Cancer Campus, 94800 Villejuif, France
[8]Pôle de Biologie, Hôpital Européen Georges Pompidou, AP-HP, 75015 Paris, France
[9]Department of Women's and Children's Health, Karolinska University Hospital, 17176 Stockholm, Sweden
[10]Department of Oncology, The Second Xiangya Hospital, Central South University, Hunan, China
[11]These authors contributed equally
[12]Lead contact
*Correspondence: xieyangchun88@csu.edu.cn (Y.X.), daolin.tang@utsouthwestern.edu (D.T.)
https://doi.org/10.1016/j.celrep.2021.108767

SUMMARY

Although induction of ferroptosis, an iron-dependent form of non-apoptotic cell death, has emerged as an anticancer strategy, the metabolic basis of ferroptotic death remains poorly elucidated. Here, we show that glucose determines the sensitivity of human pancreatic ductal carcinoma cells to ferroptosis induced by pharmacologically inhibiting system xc^-. Mechanistically, SLC2A1-mediated glucose uptake promotes glycolysis and, thus, facilitates pyruvate oxidation, fuels the tricyclic acid cycle, and stimulates fatty acid synthesis, which finally facilitates lipid peroxidation-dependent ferroptotic death. Screening of a small interfering RNA (siRNA) library targeting metabolic enzymes leads to identification of pyruvate dehydrogenase kinase 4 (PDK4) as the top gene responsible for ferroptosis resistance. PDK4 inhibits ferroptosis by blocking pyruvate dehydrogenase-dependent pyruvate oxidation. Inhibiting PDK4 enhances the anticancer activity of system xc^- inhibitors *in vitro* and in suitable preclinical mouse models (e.g., a high-fat diet diabetes model). These findings reveal metabolic reprogramming as a potential target for overcoming ferroptosis resistance.

INTRODUCTION

Physiological cell death plays fundamental roles in animal development and tissue homeostasis, whereas pathological cell death is implicated in development of many inflammatory diseases as well as in the pathogenesis of cancer (Vanden Berghe et al., 2014). Generally, cell death is divided into two types: accidental cell death and regulated cell death (Galluzzi et al., 2018). Regulated cell death is subdivided into apoptotic and non-apoptotic forms, which exhibit different regulatory mechanisms and signaling pathways (Tang et al., 2019). The propensity of cancer cells to die is affected by metabolic reprogramming, one of the hallmarks of cancer (Hanahan and Weinberg, 2011).

Knowledge regarding cancer metabolism (DeBerardinis and Chandel, 2016; Pavlova and Thompson, 2016), especially with respect to reprogramming glucose metabolism (Hay, 2016), has progressed rapidly and is providing potential biomarkers and therapeutic targets. Compared with normal cells, cancer cells consume more glucose to support their anabolic requirements (Vander Heiden et al., 2009) and augment their resistance to anticancer drugs (Zaal and Berkers, 2018). However, our knowledge about the contribution of glucose metabolism to regulation of non-apoptotic regulated cell death is rather limited.

Ferroptosis is an iron-dependent form of non-apoptotic cell death driven by lipid peroxidation (Chen et al., 2020b) that is typically triggered by inhibiting antioxidant systems, in particular the cystine/glutamate antiporter system xc^- (Dixon et al., 2012) and glutathione peroxidase 4 (GPX4) (Yang et al., 2014). Ferroptotic responses occur in the context of a complex triangular relationship between pathological cell death, inflammatory responses, and immune reactions (Stockwell et al., 2017; Tang et al., 2020; Xie et al., 2016a). In recent years, ferroptosis has been attributed major potential for cancer therapy (Chen et al., 2021b; Friedmann Angeli et al., 2019; Hassannia et al., 2019). For example, deletion of *Slc7a11*, a system xc^- subunit, induces ferroptotic death and inhibits pancreatic ductal adenocarcinoma

(PDAC) growth in mice (Badgley et al., 2020). Nonetheless, the molecular mechanism underlying resistance to ferroptosis-inducing agents is poorly understood.

In the present study, we examined how glucose regulates ferroptotic cell death and its implications for tumor therapy. We found that glucose deprivation selectively blocked system xc^- inhibitor-induced but not GPX4 inhibitor-mediated ferroptosis in human PDAC cells. Small interfering RNA (siRNA) library-based screening led to identification of pyruvate dehydrogenase kinase 4 (PDK4) as a driver of ferroptosis resistance. Indeed, PDK4 can block pyruvate dehydrogenase-mediated fueling of glucose-derived pyruvate oxidation into the tricarboxylic acid (TCA) cycle and subsequent fatty acid synthesis. Targeting PDK4-dependent metabolic pathway enhances system xc^- inhibitor-induced tumor suppression *in vitro* and *in vivo*. Our findings establish a previously unidentified regulatory role of PDK4 in ferroptosis.

RESULTS

SLC2A1-dependent glucose uptake facilitates ferroptosis

Erastin was first identified by synthetic lethal high-throughput screening (Dolma et al., 2003) and is now recognized as a classic ferroptosis inducer. Mechanistically, erastin mainly acts to inhibit system xc^-, depleting cytoprotective glutathione (GSH) (Dixon et al., 2012). To determine the role of glucose in ferroptosis, we first measured erastin-induced cell death in two human PDAC cell lines (PANC1 and MIAPaCa2) and primary human PDAC cells (which we will refer to here as pHsPDACs) cultured in commercially available high-glucose (4,500 mg/L, approximately 25 mM) or no-glucose medium. Other components, including amino acids, vitamins, inorganic salts, and serum, were the same in the high-glucose and no-glucose medium. Erastin dose-dependently reduced cell viability in high-glucose medium but not in no-glucose medium (Figure 1A). Similar results were obtained when human PDAC cells were treated with sulfasalazine (SAS) (Figure 1A), a clinically approved system xc^- inhibitor (Gout et al., 2001). In contrast, glucose deprivation had no significant effect on GPX4 inhibitor-induced (e.g., RSL3 and FIN56) cell growth inhibition (Figure 1A). Consistent with previous studies (El Mjiyad et al., 2011; Muñoz-Pinedo et al., 2003), glucose deprivation increased apoptosis induced by staurosporine (STS) and triggered cell growth inhibition (Figure 1A). Supplementation with exogenous glucose dose-dependently restored ferroptosis sensitivity, whereas it increased STS resistance in PDAC cells cultured in initially glucose-free medium (Figure 1A). Ferroptosis inhibitors (e.g., liproxstatin-1 [Friedmann Angeli et al., 2014], ferrostatin-1 [Yang et al., 2014], and baicalein [Xie et al., 2016b]), but not apoptosis inhibitors (e.g., Z-VAD-FMK and Z-DEVD-FMK), blocked this glucose-dependent cell death in PANC1 cells responding to erastin or SAS (Figure S1A).

To examine the effect of glucose on lipid metabolism, we performed an untargeted lipidomics analysis in PANC1 cells. This assay identified 275 lipid species that were downregulated (>50%, $p < 0.05$) in PANC1 cells cultured in glucose-free medium compared with high-glucose medium (Figure S1B). Among them, phosphatidylcholine and phosphatidylethanolamine, the phospholipids used in ferroptosis (Gaschler et al., 2018; Kagan et al., 2017), were significantly downregulated by glucose-free medium (Figure S1B). Compared with RSL3, glucose-free medium further limited upregulation of lipid species (e.g., PC and PE) induced by erastin (Figure S1C). Glucose-free medium also inhibited ferroptotic cell death caused by cystine depletion (Figure S1D). These findings suggest a distinct role of glucose in control of system xc^- inhibitor-induced ferroptosis compared with GPX4 inhibitor-induced ferroptosis.

The arachidonate lipoxygenase (ALOX) family plays a tissue- or cell-dependent role in induction of ferroptosis via generation of lipid peroxide (Chen et al., 2020a). Small hairpin RNA (shRNA)-mediated knockdown of *ALOX5* (Figure S1E), an ALOX family member expressed in pancreatic cancer cells (Li et al., 2020a), also prevented glucose-dependent cell death in PANC1 cells in response to erastin or SAS (Figure S1F), indicating that ALOX5 is required for system xc^- inhibitor-induced ferroptosis under high-glucose conditions.

Because glucose transporters, also known as the SLC2A or GLUT family, facilitate transport of glucose across a plasma membrane in a cell type- and tissue context-dependent manner (Thorens and Mueckler, 2010), we examined their expression in PDAC cells. Among 14 human SLC2A family members, mRNA expression of *SLC2A1* and *SLC2A3* was upregulated in PANC1, MIAPaCa2, and pHsPDAC cells following treatment with erastin or SAS, but not with RSL3, FIN56, or STS, in high-glucose medium (Figure S2). siRNA-mediated knockdown of *SLC2A1* (Figure S3A), but not *SLC2A3* (Figure S3A), inhibited erastin- or SAS-induced glucose uptake (Figure 1B), GSH reduction (Figure 1C), and cell death (Figure 1D) in PANC1 and MIAPaCa2 cells in high-glucose medium, indicating a role of SLC2A1-dependent glucose uptake in mediating system xc^- inhibitor-induced ferroptosis in PDAC cells.

Consequently, knockdown of *SLC2A1*, but not *SLC2A3*, blocked erastin- or SAS-induced lipid peroxidation, as measured with the fluorescent biosensor C11-BODIPY (Figure 1E) or by quantifying malondialdehyde (MDA) (Figure 1F). Although the ferroptosis activators erastin and SAS have the ability to cause intracellular iron uptake through multiple mechanisms (Bogdan et al., 2016), erastin- or SAS-induced Fe^{2+} (ferrous iron) accumulation was not affected by knockdown of *SLC2A1* or *SLC2A3* (Figure S3B). Moreover, erastin- or SAS-induced mRNA expression of iron metabolism-associated genes (e.g., ferritin heavy chain 1 [*FTH1*], ferritin light chain [*FTL*], transferrin receptor [*TFRC*], solute carrier family 11 member 2/divalent metal transporter 1 [*SLC11A2/DMT1*], and solute carrier family 40 member 1/ferroportin1 [*SLC40A1/FPN1*]) were not affected by suppression of SLC2A1 or SLC2A3 in PANC1 cells (Figure S3C). These findings suggest that increased lipid peroxidation, but not iron accumulation, is likely to be responsible for high glucose-dependent ferroptosis.

Pyruvate oxidation-dependent fatty acid synthesis facilitates ferroptosis

Even under normoxic conditions, cancer cells maintaining high glycolytic flux to produce pyruvate and lactate (Alfarouk et al., 2014). Biochemical assay showed that the levels of pyruvate (Figure 2A) and lactate (Figure 2B) were upregulated in PANC1

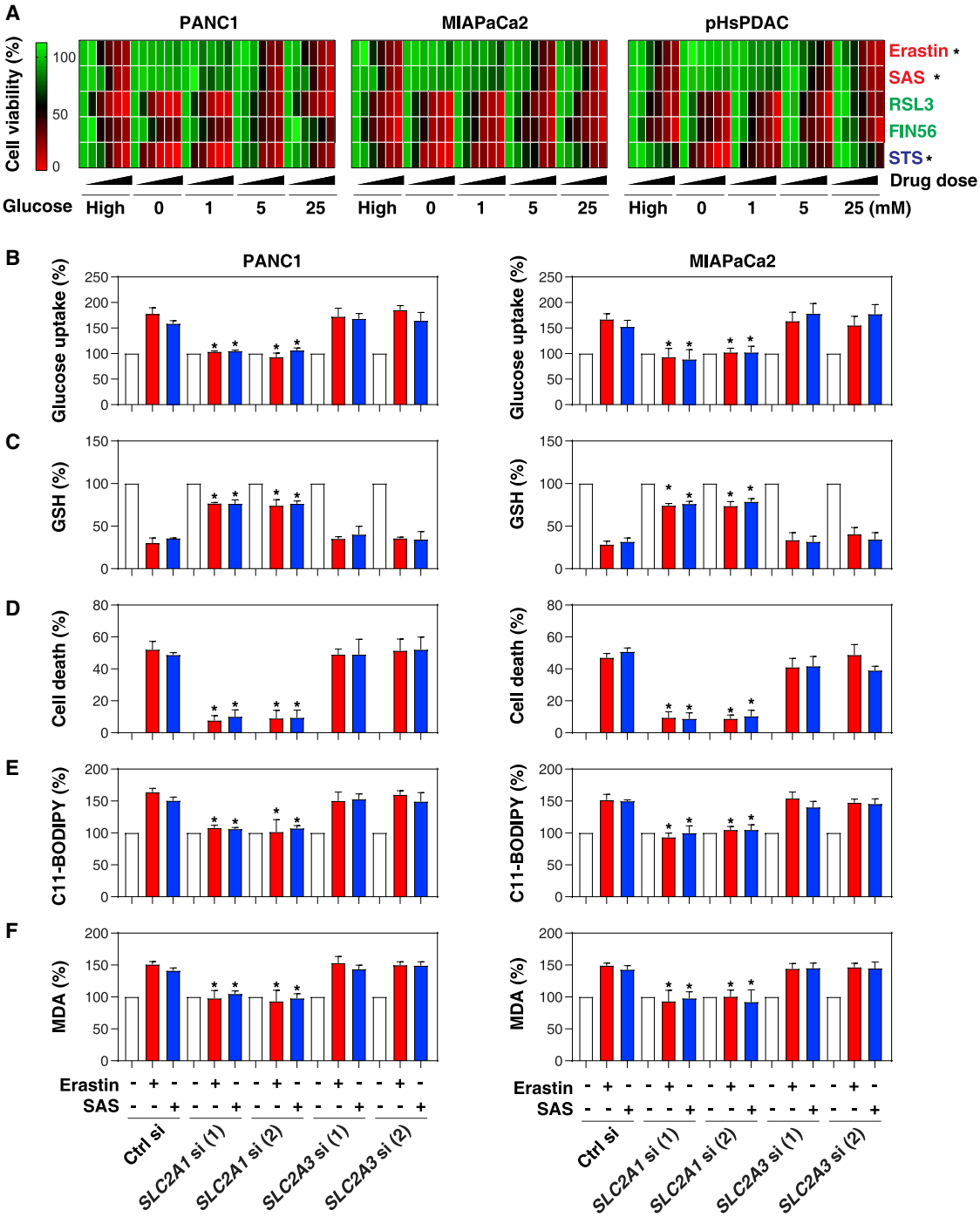

Figure 1. SLC2A1-dependent glucose uptake facilitates ferroptosis

(A) Heatmap of cell viability in human PDAC cell lines (PANC1 and MIAPaCa2) or primary cells (pHsPDAC) following treatment with erastin (0, 1.25, 2.5, 5, 10, and 20 μM), sulfasalazine (SAS; 0, 0.125, 0.25, 0.5, 1, and 2 mM), RSL3 (0, 0.125, 0.25, 0.5, 1, and 2 μM), FIN56 (0, 0.625, 1.25, 2.5, 5, and 10 μM), or staurosporine (STS; 0, 0.125, 0.25, 0.5, 1, and 2 μM) in the indicated glucose-dependent medium for 24 h. Cell viability was normalized to the DMSO control (0.01%) as 100%. There were significant differences in inhibition of cell viability induced by erastin, SAS, and STS between the no-glucose group and high-glucose group, the no-glucose group and no-glucose + 5 mM glucose group, and the no-glucose group and no-glucose + 25 mM glucose group (n = 3 biologically independent samples; *$p < 0.05$, two-way ANOVA with Tukey's multiple comparisons test).

(B–F) Relative levels of glucose uptake (B), GSH (C), cell death (D), C11-BODIPY (E), and MDA (F) in control, *SLC2A1* knockdown or *SLC2A3* knockdown PANC1 and MIAPaCa2 cells following treatment with erastin (10 μM) or SAS (1 mM) for 24 h in high-glucose medium (n = 3 biologically independent samples; *$p < 0.05$ versus the control siRNA group, two-way ANOVA with Tukey's multiple comparisons test). Data were normalized to the DMSO control (0.01%) as 100%. Data are presented as mean ± SD. See also Figures S1–S3.

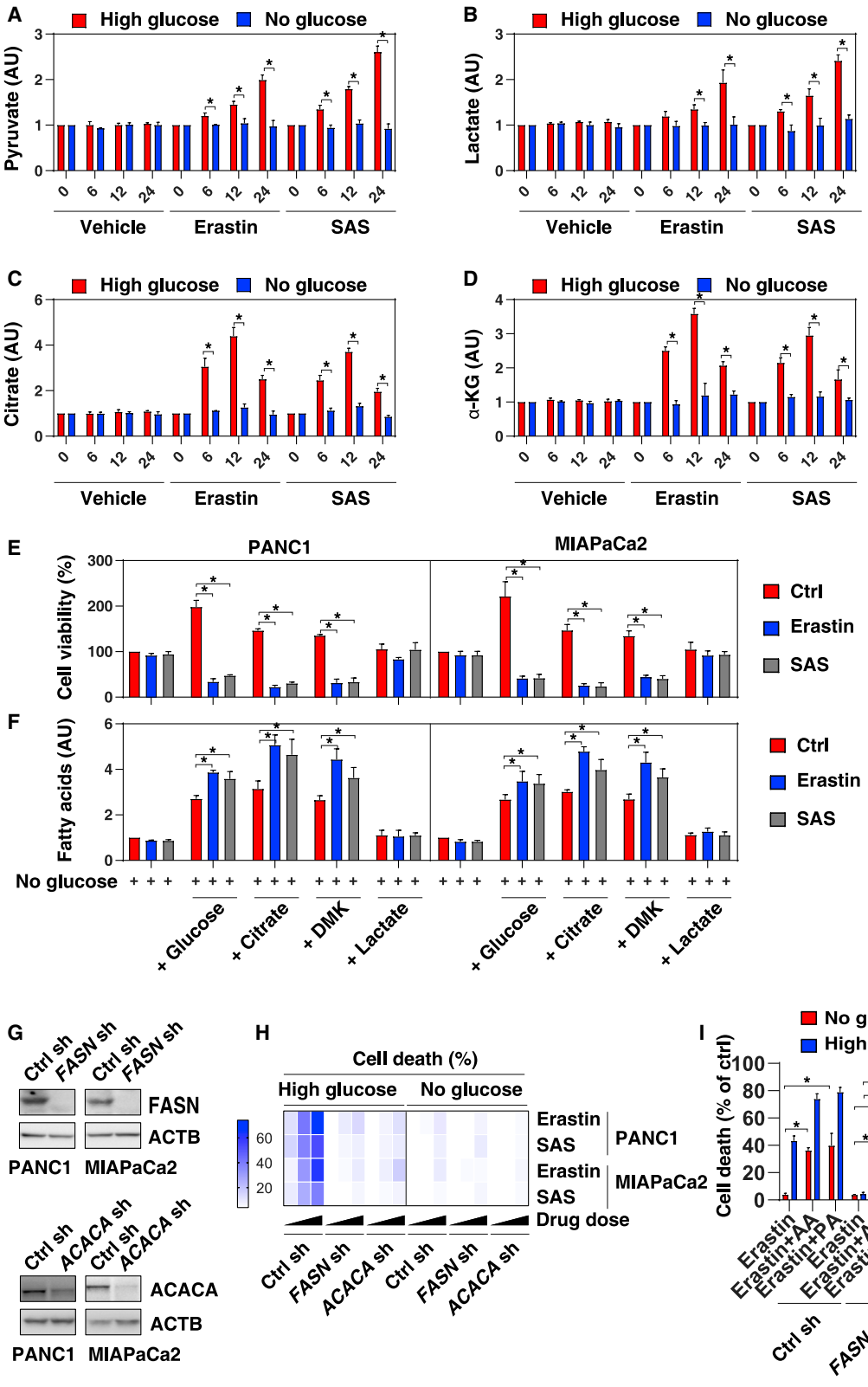

(legend on next page)

cells by erastin or SAS in high-glucose medium but not in no-glucose medium. In addition to reduction of pyruvate to lactate, pyruvate can be oxidized to acetyl-coenzyme A (CoA) to enter the TCA cycle to form citrate, leading to metabolic flexibility (Olson et al., 2016). Kinetic studies revealed that the levels of citrate (Figure 2C) as well as those of its downstream production α-ketoglutarate (α-KG) (Figure 2D) were upregulated in PANC1 cells by erastin or SAS in high-glucose medium but not in no-glucose medium.

We next sought to determine whether the main outcomes of pyruvate metabolism play an equally effective role in ferroptosis. Addition of citrate or α-KG (administered as its cell-permeable precursor dimethyl-α-KG [DMK]), but not lactate, restored erastin- or SAS-induced cell viability inhibition in PANC1 and MIAPaCa2 cells under glucose deprivation conditions (Figure 2E). These observations suggest that pyruvate-mediated TCA cycle activation, but not pyruvate-mediated lactate production, may promote ferroptosis.

α-KG can be generated from glycolysis (via pyruvate) as well as from glutamine anaplerosis (Altman et al., 2016). Addition of excessive glutamate or glutamine to glucose-free medium restored cellular ferroptosis sensitivity (Figure S4A), commensurate with an increase in intracellular α-KG (Figure S4B) and citrate (Figure S4C), supporting the notion that an alternative glutamine metabolic pathway also contributes to ferroptosis by activating the TCA cycle in mitochondria (Gao et al., 2015, 2019).

Pyruvate oxidation is an important intermediate step in conversion of glucose into fatty acids through citrate (DeBerardinis and Chandel, 2016; Pavlova and Thompson, 2016). Because synthesis of fatty acids, especially polyunsaturated fatty acids (PUFAs), is required for ferroptosis (Doll et al., 2017; Kagan et al., 2017; Yuan et al., 2016), we quantified the levels of intracellular free fatty acids. We found that glucose depletion inhibited erastin- or SAS-induced fatty acid generation, an effect that was reversed by addition of glucose or, alternatively, citrate, DMK, glutamate, or glutamine but not by lactate (Figure 2F; Figure S4D). These results indicate that pyruvate-mediated TCA cycle activation is required for fatty acid production during glucose-dependent ferroptosis.

Next we suppressed expression of acetyl-CoA carboxylase alpha (ACACA/ACC) and fatty-acid synthase (FASN), two enzymes of fatty acid synthesis downstream of citrate production (Röhrig and Schulze, 2016). Like glucose depletion, knockdown of *FASN* or *ACACA* by suitable shRNAs (Figure 2G) inhibited erastin- or SAS-induced cell death (Figure 2H), and this process was associated with decreased MDA production (Figure S5A), but no changes in Fe^{2+} accumulation (Figure S5B), in PANC1 and MIAPaCa2 cells under high-glucose conditions. Moreover, exogenous PUFAs (e.g., arachidonic acid [C20:4]) or palmitic acid (C16:0, the direct product of ACACA/FASN activation) (Menendez and Lupu, 2007) restored the sensitivity of *FASN* knockdown or *ACACA* knockdown PANC1 cells to erastin under high-glucose or no-glucose conditions (Figure 2I). Our findings demonstrate that TCA-mediated fatty acid synthesis is required for system xc^- inhibitor-induced lipid peroxidation and subsequent ferroptotic death in PDAC cells.

PDK4 is a key regulator of ferroptosis resistance

There are four basic pathways of glucose metabolism: glycolysis, gluconeogenesis, glycogenesis, and glycogenolysis, which may engage in complex crosstalk and feedback loops with other nutrient metabolism pathways (Röder et al., 2016). To identify the core gene of glucose metabolism responsible for system xc^- inhibitor resistance, we used a siRNA library targeting 87 glucose metabolism-associated genes. Knockdown of *PDK4* (a repressor of the conversion of pyruvate into acetyl-CoA by the PHD complex) had the strongest sensitizing effect with respect to erastin-mediated killing of PANC1 cells in no-glucose medium (Figure 3A). Other genes whose knockdown conferred erastin sensitivity included those coding for isocitrate dehydrogenase 1 (also known as nicotinamide adenine dinucleotide phosphate [NADP] (+) 1 or IDH1; it catalyzes oxidative decarboxylation of isocitrate to α-KG) and phosphoenolpyruvate carboxykinase 1 (“PCK1,” a gluconeogenic enzyme responsible for conversion of oxaloacetate to phosphoenolpyruvate) (Figure 3A). In contrast, knockdown of other isoforms of PDK (*PDK1*, *PDK2*, and *PDK3*), IDH (*IDH2*, *IDH3A*, and *IDH3B*), and PCK (*PCK2*) by siRNA (Figure 3B) failed to restore erastin- or SAS-induced cell death in PANC1 and MIAPaCa2 cells cultured in no-glucose medium (Figure 3C). Consistent with the cell death results, knockdown of *PDK4*, *IDH1*, or *PCK1*, but not of their isoforms, restored erastin- or SAS-induced citrate production (Figure 3D), fatty acid production (Figure 3E), and MDA production (Figure 3F) in PANC1 and MIAPaCa2 cells under no-glucose conditions. These findings further support the hypothesis that glucose-dependent pyruvate oxidation, coupled to other metabolic pathways, may promote ferroptosis in PDAC cells.

Figure 2. Pyruvate oxidation-dependent fatty acid synthesis facilitates ferroptosis

(A–D) Relative intracellular levels of pyruvate (A), lactate (B), citrate (C), and α-KG (D) in PANC1 cells following treatment with vehicle, erastin (10 μM), or SAS (1 mM) for 6–24 h in high-glucose or no-glucose medium (n = 3 biologically independent samples; *p < 0.05, two-way ANOVA with Tukey’s multiple comparisons test; data are presented as mean ± SD).

(E and F) Relative levels of cell viability (E) and intracellular fatty acids (F) in PANC1 and MIAPaCa2 cells following treatment with erastin (10 μM) or SAS (1 mM) for 24 h in no-glucose medium in the absence or presence of glucose (25 mM), citrate (10 mM), DMK (7 mM), or lactate (25 mM) (n = 3 biologically independent samples; *p < 0.05, two-way ANOVA with Tukey’s multiple comparisons test; data are presented as mean ± SD).

(G) Western blot analysis of the indicated protein expression in control, *FASN* knockdown, or *ACACA* knockdown PANC1 and MIAPaCa2 cells.

(H) Heatmap of relative cell death in control, *FASN* knockdown, or *ACACA* knockdown PANC1 and MIAPaCa2 cells following treatment with erastin (0, 10, and 20 μM) or SAS (0, 1, and 2 mM) in high-glucose or no-glucose medium for 24 h.

(I) Cell death analysis of the indicated PANC1 cells following treatment with erastin (10 μM) for 24 h in high-glucose or no-glucose medium in the absence or presence of arachidonic acid (AA, 250 μM) or palmitic acid (PA, 250 μM) (n = 3 biologically independent samples; *p < 0.05, two-way ANOVA with Tukey’s multiple comparisons test; data are presented as mean ± SD).

See also Figures S4–S5.

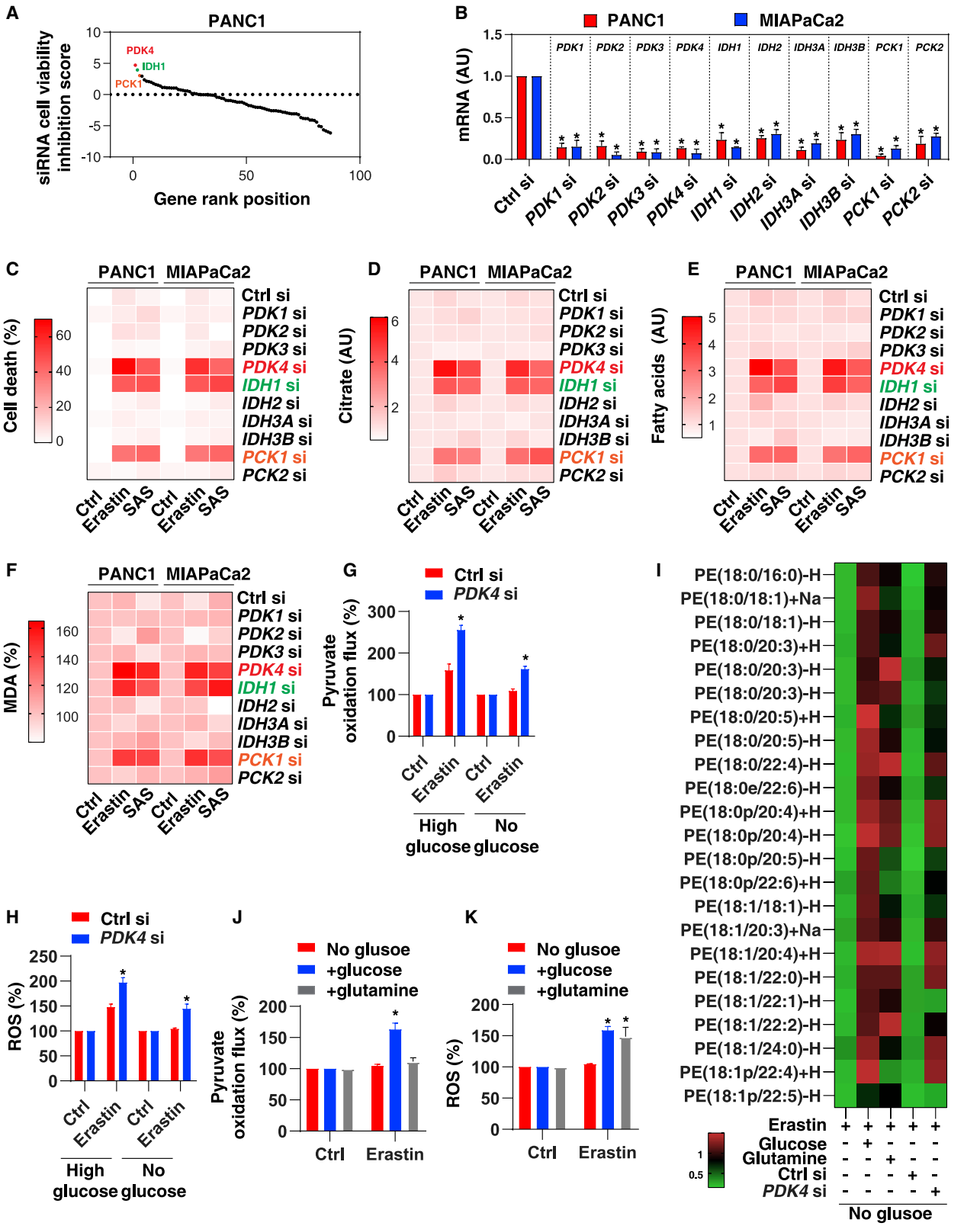

(legend on next page)

Next we focused on the effects of *PDK4* knockdown on pyruvate oxidation flux, reactive oxygen species (ROS) production, and synthesis of PE-PUFAs. Oxidized PE-PUFAs (e.g., arachidonic acid [C20:4] and adrenic acid [C22:4]) are believed to play a direct role in promoting ferroptosis (Kagan et al., 2017). Knockdown of *PDK4* increased erastin-induced pyruvate oxidation flux (Figure 3G) and ROS production (Figure 3H) in PANC1 cells under high-glucose and no-glucose conditions. In addition, knockdown of *PDK4* restored erastin-induced PE-PUFA production (including arachidonic acid and adrenic acid) in the absence of glucose (Figure 3I). Different from addition of glucose, addition of excessive glutamine to glucose-free medium failed to restore pyruvate oxidation flux (Figure 3J), although it increased ROS production (Figure 3K) and synthesis of PE-PUFAs in erastin-treated PANC1 cells (Figure 3I). These findings indicate that two different upstream pathways (pyruvate oxidation and glutamine anaplerosis) enter the TCA cycle to increase ROS production and induce PE-PUFA synthesis for ferroptosis.

PDK4 represses pyruvate oxidation via inhibition of pyruvate dehydrogenase (PDH; a complex of three enzymes that converts pyruvate into acetyl-CoA) and, hence, influences the switch from glucose metabolism to fatty acid synthesis (Saunier et al., 2016; Sradhanjali and Reddy, 2018). Erastin or SAS inhibited PDK4 protein expression under high-glucose conditions but not under no-glucose conditions, as determined by immunoblot (Figure 4A). RSL3 and FIN56 failed to affect PDK4 expression under high-glucose conditions (Figure 4A). Moreover, knockdown of *SLC2A1* diminished high glucose-dependent PDK4 downregulation (Figure 4A), indicating that SLC2A1-dependent PDK4 expression may decide glucose-dependent ferroptosis activity.

To further investigate the effects of PDK4 on ferroptosis, we generated *PDK4*-overexpressing PDAC cells (PANC1 and MIAPaCa2) (Figure 4B). Similar to glucose deprivation (Figure 1), overexpression of *PDK4* blocked erastin- or SAS-induced PDH activity (Figure 4C), citrate production (Figure 4D), fatty acid production (Figure 4E), MDA production (Figure 4F), and cell death (Figure 4G) in PDAC cells cultured under high-glucose conditions. Similar to overexpression of *PDK4*, knockdown of *PDHA1* (a functional subunit of the PDH complex) led to ferroptosis resistance in PANC1 and MIAPaCa2 cells following erastin or SAS treatment under high-glucose conditions (Figures 4H and 4I). These findings suggest that PDK4 restrains glucose-dependent ferroptosis.

Because pyruvate can also enter the TCA cycle through pyruvate carboxylase (PC)-mediated oxaloacetate production (Jitrapakdee et al., 2008), we inhibited expression of PC in PANC1 cells using specific shRNAs (Figure 4H). Unlike knockdown of *PDHA1*, knockdown of *PC* failed to affect erastin- or SAS-induced ferroptosis (Figure 4I). These findings suggest that PDH-mediated pyruvate oxidation (rather than PC-mediated pyruvate metabolism entry into the TCA cycle) promotes ferroptosis. Moreover, knockdown of *ACACA* reversed erastin- or SAS-induced ferroptosis in *PDK4*-knockdown PANC1 cells, indicating that PDK4 regulates ferroptosis in an ACACA-dependent manner (Figure 4J). Knockdown of *PDK4* did not significantly affect mRNA expression of certain ferroptosis regulators, such as apoptosis-inducing factor mitochondria associated 2 (*AIFM2*/*FSP1*; a negative regulator of ferroptosis by producing reduced coenzyme Q10 or increasing membrane repair; Bersuker et al., 2019; Dai et al., 2020d; Doll et al., 2019), tumor protein D52 (*TPD52*; a negative regulator of ferroptosis by increasing the formation of lipid droplets; Bai et al., 2019), charged multivesicular body protein 5 (*CHMP5*; a negative regulator of ferroptosis by increasing plasma membrane repair; Dai et al., 2020c), guanosine triphosphate (GTP) cyclohydrolase 1 (*GCH1*; a negative regulator of ferroptosis by increasing tetrahydrobiopterin production; Kraft et al., 2020), Yes1-associated transcriptional regulator (*YAP1*; a positive regulator of ferroptosis by inhibiting cell adhesion; Wu et al., 2019), nuclear factor erythroid 2-like 2 (*NFE2L2*/*NRF2*; a key regulator of antioxidant response during ferroptosis; Sun et al., 2016), and tumor protein p53 (*TP53*; a dual regulator of ferroptosis depending on its target gene and binding partner; Jiang et al., 2015; Tarangelo et al., 2018; Xie et al., 2017a) in PANC1 cells following erastin or SAS treatment (Figure 4K).

A recent study showed that glucose depletion prevents ferroptosis caused by erastin and RSL3 in immortalized mouse embryonic fibroblasts (MEFs) by activating AMP-activated protein kinase (AMPK)-mediated phosphorylation of acetyl-CoA carboxylase (Lee et al., 2020). In contrast, AMPK-mediated phosphorylation of Beclin 1 promotes ferroptotic cell death in colon cancer cells (e.g., PANC1; Song et al., 2018a) and non-cancer cells (e.g., HTR8/Svneo; Han et al., 2020)). Moreover, AMPK-mediated stearoyl-CoA desaturase (SCD/SCD1) downregulation promotes ferroptosis in hepatocellular carcinoma cells by inhibiting production of monounsaturated fatty acids (MUFAs) (Zhao et al., 2020). Interestingly, knockdown of *PDK4* increased AMPK kinase activity following treatment with erastin or RSL3 in PANC1 cells (Figure 4L). Potential AMPK inhibitors, such as dorsomorphin (also known as compound C; Dasgupta and Seibel, 2018) and MT47-100 (Scott et al., 2015), reversed erastin- or RSL3-induced cell death in *PDK4* knockdown PANC1 cells (Figure 4M). *Ampk*α*1*/α*2*$^{-/-}$ MEFs (but not *Pdk4* knockdown MEFs) were sensitive to erastin- or RSL3-induced

Figure 3. Identification of glucose metabolism genes regulating ferroptosis sensitivity

(A) siRNA library-based screening of glucose metabolism genes restoring cell viability inhibition in PANC1 cells following treatment with erastin (10 μM) for 24 h in no-glucose medium.

(B) qPCR analysis of gene expression in the indicated gene knockdown PANC1 and MIAPaCa2 cells (n = 3 biologically independent samples; *p < 0.05, one-way ANOVA with Tukey's multiple comparisons test; data are presented as mean ± SD).

(C–F) Heatmap of relative levels of cell death (C), citrate (D), fatty acids (E), and MDA (F) in control and the indicated gene knockdown PANC1 and MIAPaCa2 cells following treatment with erastin (10 μM) or SAS (1 mM) for 24 h in no-glucose medium. Data were normalized to the DMSO control (0.01%).

(G–K) Analysis of pyruvate oxidation flux, ROS production, and synthesis of PE-polyunsaturated fatty acids (PUFAs) in the indicated erastin-treated (10 μM) PANC1 cells under high-glucose or no-glucose conditions (n = 3 or 6 biologically independent samples; *p < 0.05 versus the control group, two-way ANOVA with Tukey's multiple comparisons test; data are presented as mean ± SD). Data were normalized to the DMSO control (0.01%) as 100%.

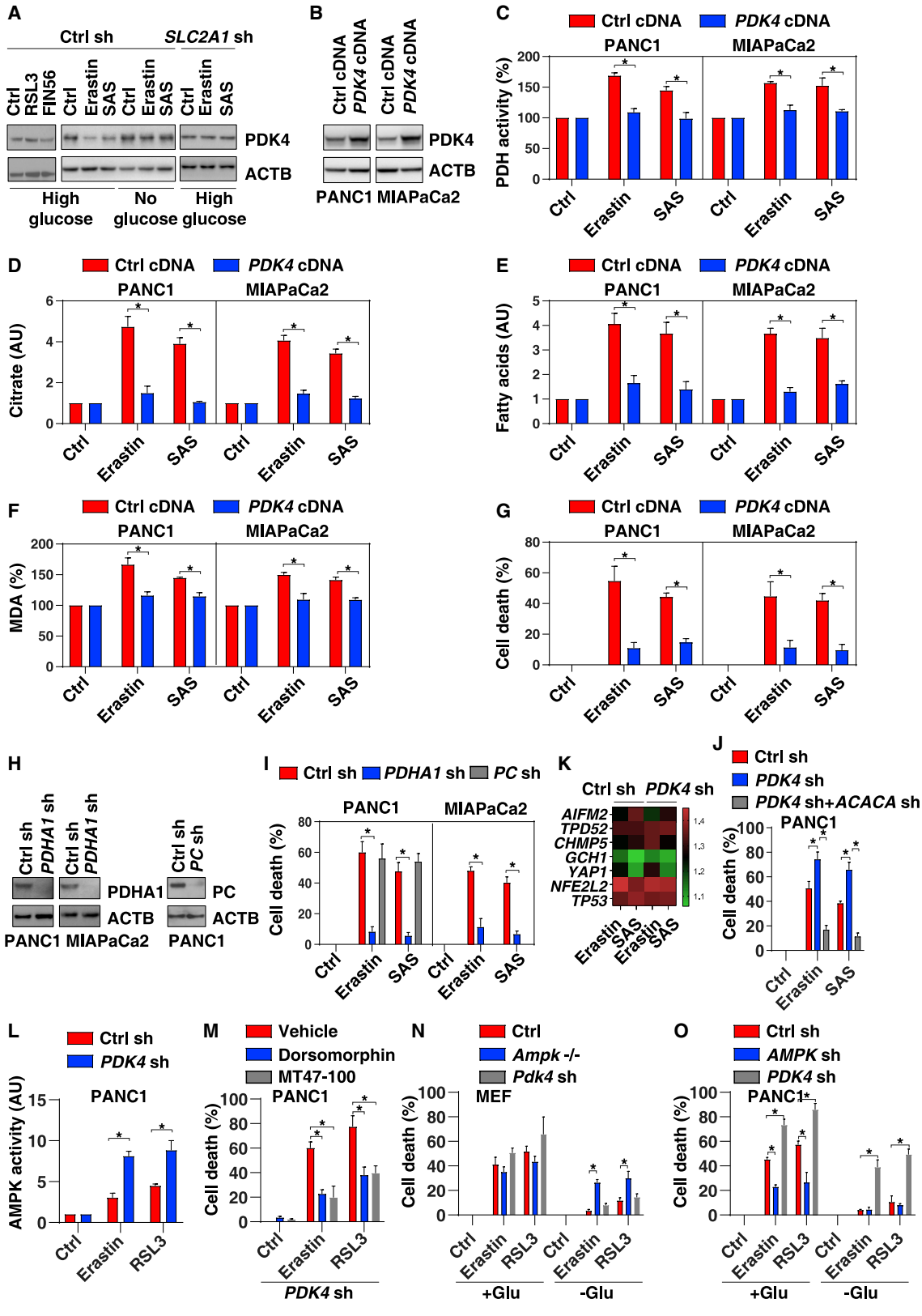

(legend on next page)

cell death under glucose starvation but not high-glucose conditions (Figure 4N). In addition, *AMPKα1/α2* knockdown PANC1 cells were resistant to erastin- or RSL3-induced cell death under high-glucose conditions but not under glucose starvation (Figure 4O). The average RNAi efficiency of target genes (AMPKα1/α2 or PDK4) in PANC1 and/or MEFs was greater than 90%. These findings indicate that the role of AMPK and PDK4 in ferroptosis is cell type dependent and that there is a complex relationship between energy status and ferroptosis induction by different activators.

A high-fat diet promotes ferroptotic cell death *in vivo*

Next we investigated whether a hyperglycemia condition might enhance the anticancer activity of imidazole ketone erastin (IKE), a metabolically stable analog of erastin (Zhang et al., 2019), *in vivo*. We used a classic high-fat diet mouse model to simulate type 2 diabetes and hyperglycemia. At 6 weeks of age, male C57BL/6J mice received a standard diet (SCD) or high-fat diet (HFD) for 12 weeks. As expected, the body weight (26.78 ± 0.8 g in the SCD group versus 37.7 ± 1.5 g in the HFD group, $p < 0.05$) and blood glucose levels (100.6 ± 3.46 mg/dL in the SCD group versus 148.9 ± 3.61 mg/dL in the HFD group, $p < 0.05$) of HFD mice were upregulated compared with SCD mice. Then the mouse PDAC cell line KPC was implanted subcutaneously into the right abdomen of SCD and HFD mice. One week later, tumor-bearing mice were treated with IKE (40 mg/kg, intraperitoneally [i.p.], once every other day), the ferroptosis inhibitor liproxstatin-1 (10 mg/kg, i.p., once every other day), or the PDK inhibitor dichloroacetate (DCA, 50 mg/kg, i.p., once every other day) with the corresponding diet. After 3 weeks of treatment, IKE-mediated tumor suppression in the HFD group was greater than in the SCD group (Figure 5A). DCA further enhanced the anti-cancer activity of IKE in the SCD and HFD groups. This HFD- or DCA-mediated effect was associated with increased levels of intra-tumoral MDA (Figure 5B), mRNA expression of prostaglandin-endoperoxide synthase 2 (*Ptgs2*; a marker of ferroptosis *in vivo*; Chen et al., 2021a; Yang et al., 2014; Figure 5C) and elevated plasma concentrations of high-mobility group box 1 (HMGB1; a protein that is released from ferroptotic cells; Chen et al., 2021a; Wen et al., 2019; Figure 5D). However, IKE did not change the activity of caspase-3 (a marker of apoptosis; Figure 5E). HFD- or DCA-mediated improvement of cancer growth control by IKE was reversed by liproxstatin-1 (Figures 5A–5D), indicating that it involves ferroptosis.

We also investigated the role of PDK4 in regulation of IKE-induced tumor suppression. KPC cells with shRNA-mediated PDK4 knockdown (*Pdk4 sh*) (Figure 6A) were more sensitive to IKE-induced tumor suppression in SCD and HFD mice (Figure 6B). This *Pdk4 sh*-conferred therapy sensitivity was associated with increased intra-tumoral MDA (Figure 6C),*Ptgs2* mRNA (Figure 6D), and plasma HMGB1 (Figure 6E). In these cells, the activity of caspase-3 was not affected by IKE (Figure 6F). The *Pdk4 sh*-mediated improvement of tumor suppression by IKE was also reversed by liproxstatin-1 (Figures 6A–6E). These preclinical studies support the hypothesis that PDK4 acts as a negative regulator of ferroptosis *in vivo*.

DISCUSSION

PDAC is a highly aggressive cancer and poorly responsive to current treatments with abnormal metabolism and degradation (Li et al., 2020b). Diabetes is often associated with PDAC (Andersen et al., 2017), and hyperglycemia may contribute to therapy resistance (Grasso et al., 2017). Therefore, targeting abnormal metabolic pathways related to glucose metabolism may provide a novel approach to kill PDAC cells. In the current study, we demonstrated that system xc^- inhibitors are particularly efficient at killing PDAC cells in a high-glucose environment. Pyruvate oxidation-mediated activation of the TCA cycle (including production of citric acid) is necessary for fatty acid synthesis and subsequent lipid peroxidation, promoting ferroptosis. This glucose-mediated sensitization to ferroptosis induction relies on pyruvate oxidation catalyzed by PDH, which is repressed by PDK4.

Figure 4. PDK4-mediated PDH inhibition promotes ferroptosis resistance

(A) Western blot analysis of PDK4 expression in the indicated PANC1 cells following treatment with erastin (10 μM) or SAS (1 mM) for 24 h in high- or no-glucose medium.

(B) Western blot analysis of PDK4 protein expression in control or *PDK4*-overexpression PANC1 and MIAPaCa2 cells.

(C–G) Relative levels of PDH activity (C), citrate (D), fatty acids (E), MDA (F), and cell death (G) in control or *PDK4*-overexpression PANC1 and MIAPaCa2 cells following treatment with erastin (10 μM) or SAS (1 mM) for 24 h in high-glucose medium (n = 3 biologically independent samples; *p < 0.05, two-way ANOVA with Tukey's multiple comparisons test; data are presented as mean ± SD). Data were normalized to the DMSO control (0.01%).

(H) Western blot analysis of PDHA1 or PC protein expression in the indicated PANC1 and MIAPaCa2 cells.

(I and J) Relative levels of cell death in control or the indicated PANC1 and MIAPaCa2 cells following treatment with erastin (10 μM) or SAS (1 mM) for 24 h in high-glucose medium (n = 3 biologically independent samples; *p < 0.05, two-way ANOVA with Tukey's multiple comparisons test; data are presented as mean ± SD). Data were normalized to the DMSO control (0.01%).

(K) Heatmap of gene expression in the indicated PANC1 cells following treatment with erastin (10 μM) or SAS (1 mM) for 24 h in high-glucose medium (data are shown as the mean of 3 biologically independent samples).

(L) Relative levels of AMPK in the indicated PANC1 cells following treatment with erastin (10 μM) or SAS (1 mM) for 24 h in high-glucose medium (n = 3 biologically independent samples; *p < 0.05, two-way ANOVA with Tukey's multiple comparisons test; data are presented as mean ± SD).

(M) Cell death in *PDK4* knockdown PANC1 cells following treatment with erastin (10 μM) or SAS (1 mM) for 24 h in the absence or presence of dorsomorphin (5 μM) or MT47-100 (20 μM) in high-glucose medium (n = 3 biologically independent samples; *p < 0.05, two way ANOVA with Tukey's multiple comparisons test; data are presented as mean ± SD).

(N) Cell death in the indicated MEFs following treatment with erastin (1 μM) or RSL3 (0.1 μM) for 24 h in high-glucose or no-glucose medium (n = 3 biologically independent samples; *p < 0.05, two-way ANOVA with Tukey's multiple comparisons test; data are presented as mean ± SD).

(O) Cell death in the indicated PANC1 cells following treatment with erastin (10 μM) or RSL3 (0.5 μM) for 24 h in high-glucose or no-glucose medium (n = 3 biologically independent samples; *p < 0.05, two-way ANOVA with Tukey's multiple comparisons test; data are presented as mean ± SD).

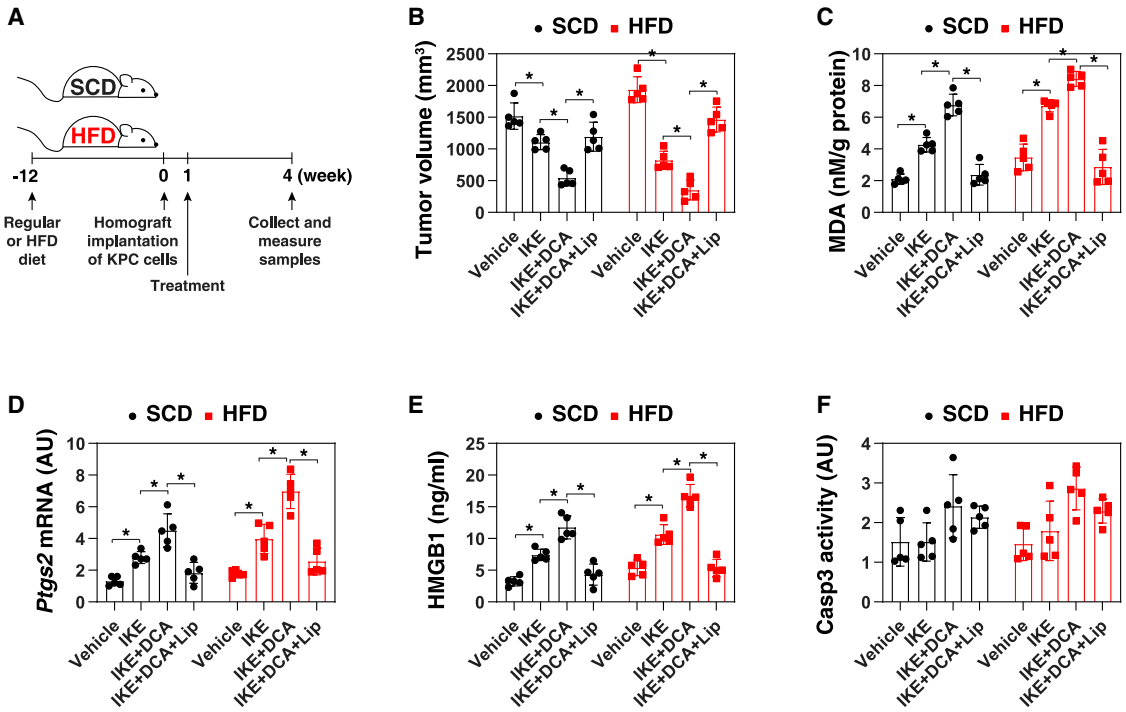

Figure 5. The PDK inhibitor DCA promotes ferroptotic cell death *in vivo*

(A) Schematic overview of therapeutic intervention studies in SCD and HFD mice. SCD or HFD mice were injected subcutaneously with KPC cells for 1 week and then treated with IKE (40 mg/kg, i.p., once every other day) in the absence or presence of the PDK inhibitor dichloroacetate (DCA; 50 mg/kg, i.p., once every other day) or liproxstatin-1 (Lip; 10 mg/kg, i.p., once every other day) on day 7 for 3 weeks.

(B–E) On day 28 after treatment, MDA levels (B) and *Ptgs2* mRNA (C) in isolated tumors and serum HMGB1 (C) were assayed (n = 5 mice/group; *p < 0.05, two-way ANOVA with Tukey's multiple comparisons test; data are presented as mean ± SD with individual data).

(F) In parallel, caspase-3 activity in isolated tumors was assayed (n = 5 mice/group; data are presented as mean ± SD with individual data).

Cell death can be executed by multiple pathways, and its deregulation can contribute to a range of human diseases, including neoplasia. Because a hallmark of cancer is the ability of malignant cells to evade apoptosis (Hanahan and Weinberg, 2011), strategies to induce non-apoptotic forms of cell death, including ferroptosis, have attracted great interest (Chen et al., 2021b; Friedmann Angeli et al., 2019; Hassannia et al., 2019). Ferroptosis was originally described as a promising therapeutic modality for targeting oncogenic *RAS* mutations (Dixon et al., 2012; Dolma et al., 2003; Yagoda et al., 2007), although recent studies indicate that it can occur in *RAS*-dependent and -independent manners (Schott et al., 2015; Xie et al., 2017a; Yu et al., 2015). The process of ferroptosis involves oxidative damage of lipid molecules resulting from an imbalance between production of ROS and antioxidant defenses (Kuang et al., 2020; Tang and Kroemer, 2020). Specifically, excessive lipid peroxidation caused by iron overload may increase membrane fluidity and permeability, which finally results in membrane rupture, a common characteristic of regulated necrosis (Feng and Stockwell, 2018). Our findings highlight the metabolic function of high glucose in promoting ferroptotic cancer cell death through lipid peroxidation but not through iron accumulation. High glucose-induced lipid peroxidation is implicated in diabetes, cardiovascular disease, and neurodegeneration (Butterfield and Halliwell, 2019; Davì et al., 2005), indicating a wider role of glucose in control of oxidative damage.

Recent research led to characterization of the fine mechanisms of ferroptosis that become ever more complex and sophisticated, involving classic and alternative pathways. In addition to a classic GSH antioxidant system composed of upstream system xc^- and the downstream enzyme GPX4, several nonclassic pathways, such as AIFM2/FSP1-dependent coenzyme Q10 production (Bersuker et al., 2019; Doll et al., 2019), endosomal sorting complexes required for transport (ESCRT)-III-mediated membrane repair (Dai et al., 2020c; Dai et al., 2020d), and Hippo pathway-related cell adhesion (Wu et al., 2019), may diminish or reduce lipid peroxidation-mediated ferroptosis in an enzyme- or nonenzyme-dependent manner. In the current study, we demonstrated that pyruvate oxidation selectively drives system xc^- inhibitor-induced (but not GPX4 inhibitor-induced) cell death in PDAC cells. Similar to our current study, a previous study showed that ferroptosis caused by systemic xc^- inhibitors (rather than GPX4 inhibitors) requires mitochondrial metabolism (Gao et al., 2019). Different tumors may express different transcripts and protein isoforms involved in glucose and lipid metabolism, which further indicates that the metabolic basis of ferroptosis may vary according to tumor type and death stimuli (Hao et al., 2018).

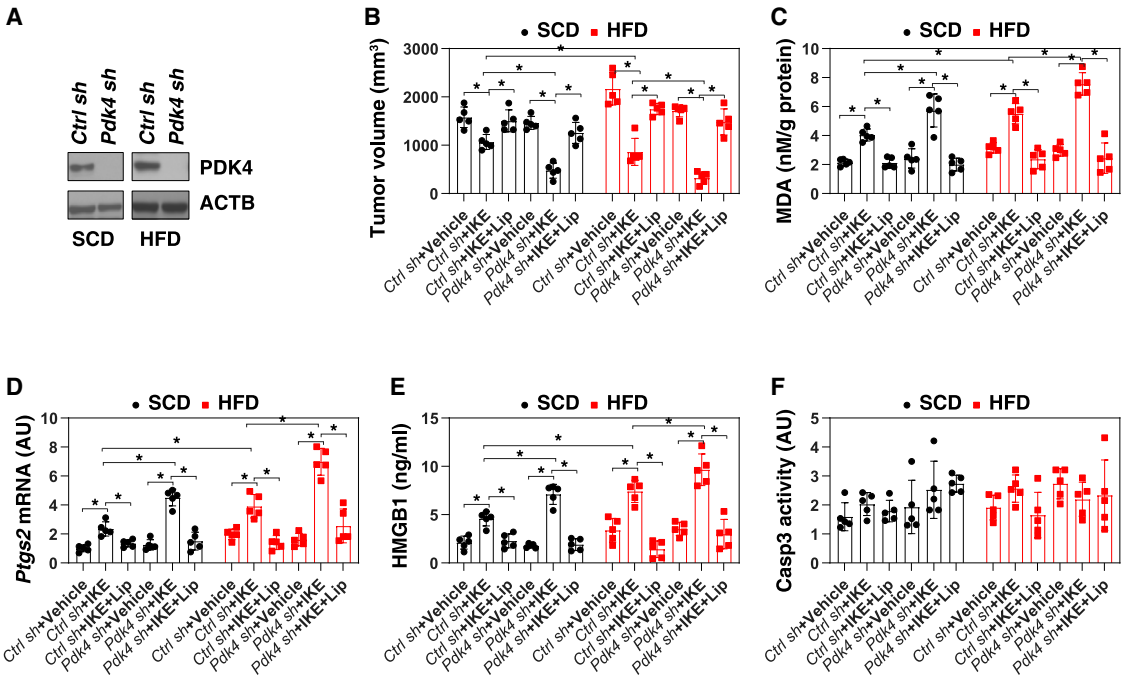

Figure 6. Knockdown of PDK promotes ferroptotic cell death *in vivo*

(A) SCD or HFD mice were injected subcutaneously with the indicated KPC cells for 1 week and then treated with IKE (40 mg/kg, i.p., once every other day) in the absence or presence of Lip (10 mg/kg, i.p., once every other day) on day 7 for 3 weeks. Shown is western blot analysis of PDK4 expression in isolated tumors from the control shRNA and PDK4 shRNA groups.

(B–E) On day 28 after treatment, MDA levels (B) and Ptgs2 mRNA (C) in isolated tumors and serum HMGB1 (C) were assayed (n = 5 mice/group; *p < 0.05, two-way ANOVA with Tukey's multiple comparisons test; data are presented as mean ± SD with individual data).

(F) In parallel, caspase-3 activity in isolated tumors was assayed (n = 5 mice/group; data are presented as mean ± SD with individual data).

Our findings uncover a previously unappreciated pathway of glucose uptake and utilization in selective regulation of ferroptosis in PDAC cells. We demonstrated that, in addition to the previously reported pentose phosphate pathway (Dixon et al., 2012), glucose-mediated pyruvate oxidation, but not pyruvate reduction, participates in system xc^- inhibitor-induced ferroptosis through citrate-mediated fatty acid synthesis in PDAC cells. Knowing that mitochondria play a context-dependent role in ferroptosis (Dixon et al., 2012; Gao et al., 2019), we found that the mitochondrial protein PDK4 acts as a ferroptosis repressor through inhibition of the PDH complex, blocking pyruvate oxidation and consequent citrate and fatty acid production in PDAC cells. To maintain a functional TCA cycle, cancer cells can use glutaminolysis to produce α-KG, which can be converted to citrate upon mitochondrial stress. Glutaminolysis-dependent α-KG production also contributes to ferroptosis in some cases (Gao et al., 2015, 2019). Thus, the dynamic interplay between glucose and glutamine metabolism may modulate ferroptosis sensitivity through an effect on the TCA cycle, the most important central metabolic pathway, which not only mediates adenosine triphosphate and ROS generation but also promotes fatty acid synthesis.

We demonstrated that SLC2A1-mediated glucose uptake inhibited expression of PDK4 in PDAC cells responding to erastin and SAS (but not RSL3 and FIN56). Although the exact mechanisms remain unknown, evidence suggests that glucose-mediated activation of AKT may inhibit PDK4 expression through inactivation of the forkhead box O (FOXO) transcription factors (e.g., FOXO3; Kwon et al., 2004; Wu et al., 2009). FOXO3 activation prevents ferroptotic death in renal tubular cells (Li et al., 2019a).

PDK4 plays a pleiotropic, context-dependent role in regulation of glucose and fatty acid metabolism. In normal tissue (e.g., muscle, brain, and adipocytes), increased PDK4 expression has been observed under conditions of hyperglycemia, glucose deprivation, and starvation (Hsieh et al., 2008; Jeoung et al., 2006; Wu et al., 1998), indicating that PDK4 acts as a nutrient sensor and regulator of glucose homeostasis. Altered PDK4 expression is also involved in lipid-related metabolic adaptations, including lipogenesis and fatty acid oxidation in normal tissue (Pettersen et al., 2019; Yamaguchi et al., 2018; Zhang et al., 2018). In tumor cells, upregulation of PDK4 mediates aerobic glycolysis (also called the Warburg effect), favoring tumor growth and apoptosis resistance (Leclerc et al., 2017; Liu et al., 2014; Wang et al., 2018; Wu et al., 2018). Although knockout of *PDK4* limits lipogenesis in the context of nonalcoholic steatohepatitis in mice (Zhang et al., 2018), knockdown of *PDK4* increases lipogenesis in liver cancer cells *in vitro* and *in vivo* (Yang et al., 2019), indicating a specific role of PDK4 in lipid metabolism of malignant cells. In the current study, we demonstrate that SLC2A1-dependent PDK4 downregulation under high-glucose conditions mediates system xc^- inhibitor-induced ferroptosis of PDAC cells through ACACA-FASN-dependent fatty acid synthesis and subsequent

ALOX5-dependent lipid peroxidation, suggesting metabolic modulation of ferroptosis.

Metabolic regulation of ferroptotic death may be distinct in different cancer cell types (Soula et al., 2020; Zheng and Conrad, 2020). For example, ALOX12, but not ALOX5 or ALOX15, facilitates TP53-induced ferroptosis in H1299 cells (human non-small cell lung cancer) (Chu et al., 2019). ALOX15, rather than ALOX12, is responsible for RSL3- or erastin-induced ferroptosis in HT1080 cells (human fibrosarcoma) (Shintoku et al., 2017). Moreover, ACACA is not essential for FIN56-induced ferroptosis in KBM7 cells (chronic myelogenous leukemia) (Dixon et al., 2015). Thus, different tumor cell types (and perhaps even heterogeneous cells within the same tumor) are likely to be differentially susceptible to ferroptosis and its modulation by metabolic enzyme inhibitors.

We establish that PDK4 acts to restrain ferroptosis, providing a potential anticancer target to amplify the ferroptotic activity of system xc^- inhibitors, in particular in the presence of high glucose. Thus, at the speculative level, individuals with PDAC and diabetes might be particularly suitable for this kind of therapeutic approach. Further identification of the metabolic sensors responsible for lipid synthesis, oxidation, and degradation will be important to understand the utility of ferroptosis for cancer therapy. Because glucose and lipid metabolism crosstalk at multiple levels (Chen et al., 2019; Saltiel and Kahn, 2001), it will be important to characterize how the metabolic flexibility of cancer cells may modulate ferroptotic responses in pancreatic tumorigenesis and therapy (Badgley et al., 2020; Dai et al., 2020a, Dai et al., 2020b; Kuang et al., 2021; Liu et al., 2021). Because ferroptosis is a type of autophagy-dependent cell death (Liu et al., 2020; Zhou et al., 2020), it is also important to understand how dysfunctional degradation pathways affect the protein levels of key metabolic regulators during ferroptosis (Chen et al., 2021c; Hou et al., 2016; Hu et al., 2021; Li et al., 2021).

STAR★METHODS

Detailed methods are provided in the online version of this paper and include the following:

- KEY RESOURCES TABLE
- RESOURCE AVAILABILITY
  - Lead contact
  - Materials availability
  - Data and code availability
- EXPERIMENTAL MODEL AND SUBJECT DETAILS
  - Mice model
  - Cell culture
- METHOD DETAILS
  - Cell viability and death assay
  - RNAi and gene transfection
  - RNAi screening
  - Q-PCR analysis
  - Western blot
  - Lactate assay
  - Pyruvate assay
  - PDH activity assay
  - α-KG assay
  - Glucose uptake assay
  - Lipid peroxidation assay
  - Iron assay
  - GSH assay
  - Fatty acid assay
  - Citrate assay
  - HMGB1 and caspase-3 assay
  - AMPK kinase assay
  - LC-MS/MS method for lipid analysis
  - Pyruvate oxidation flux assay
- QUANTIFICATION AND STATISTICAL ANALYSIS

SUPPLEMENTAL INFORMATION

Supplemental Information can be found online at https://doi.org/10.1016/j.celrep.2021.108767.

ACKNOWLEDGMENTS

We thank Dave Primm (Department of Surgery, University of Texas Southwestern Medical Center) for critical reading of the manuscript. R.K. is supported by a grant from the National Institutes of Health (R01CA211070). G.K. is supported by the Ligue Contre le Cancer (équipe labellisée); Agence National de la Recherche (ANR) – Projets blancs; ANR under the frame of E-Rare-2, the ERA-Net for Research on Rare Diseases; Association pour la recherché sur le cancer (ARC); Cancéropôle Ile-de-France; Chancelerie des universités de Paris (Legs Poix), Fondation pour la Recherche Médicale (FRM); a donation by Elior; the European Research Area Network on Cardiovascular Diseases (ERA-CVD; MINOTAUR); Gustave Roussy Odyssea, the European Union Horizon 2020 Project Oncobiome; Fondation Carrefour; the High-End Foreign Expert Program in China (GDW20171100085 and GDW20181100051), Institut National du Cancer (INCa); INSERM (HTE); Institut Universitaire de France; the Leducq Foundation; LabEx Immuno-Oncology; RHU Torino Lumière; the Seerave Foundation; SIRIC Stratified Oncology Cell DNA Repair and Tumor Immune Elimination (SOCRATE); and SIRIC Cancer Research and Personalized Medicine (CARPEM). Y.X. was supported by the National Natural Science Foundation of China (81802476).

AUTHOR CONTRIBUTIONS

The experiments were conceived and designed by X.S., Y.X., and D.T. The experiments were performed by X.S., J.L., F.K., X.C., R.K., Y.X., and D.T. The data were analyzed by X.S., Y.X., and D.T. The paper was written by X.S., Y.X., and D.T. H.J.Z. provided important reagents and materials. G.K. edited and commented on the manuscript.

DECLARATION OF INTERESTS

The authors declare no competing interests.

Received: April 23, 2020
Revised: December 29, 2020
Accepted: January 27, 2021
Published: February 23, 2021

REFERENCES

Alfarouk, K.O., Verduzco, D., Rauch, C., Muddathir, A.K., Adil, H.H., Elhassan, G.O., Ibrahim, M.E., David Polo Orozco, J., Cardone, R.A., Reshkin, S.J., and Harguindey, S. (2014). Glycolysis, tumor metabolism, cancer growth and dissemination. A new pH-based etiopathogenic perspective and therapeutic approach to an old cancer question. Oncoscience *1*, 777–802.

Altman, B.J., Stine, Z.E., and Dang, C.V. (2016). From Krebs to clinic: glutamine metabolism to cancer therapy. Nat. Rev. Cancer *16*, 619–634.

Andersen, D.K., Korc, M., Petersen, G.M., Eibl, G., Li, D., Rickels, M.R., Chari, S.T., and Abbruzzese, J.L. (2017). Diabetes, Pancreatogenic Diabetes, and Pancreatic Cancer. Diabetes *66*, 1103–1110.

Badgley, M.A., Kremer, D.M., Maurer, H.C., DelGiorno, K.E., Lee, H.J., Purohit, V., Sagalovskiy, I.R., Ma, A., Kapilian, J., Firl, C.E.M., et al. (2020). Cysteine depletion induces pancreatic tumor ferroptosis in mice. Science *368*, 85–89.

Bai, Y., Meng, L., Han, L., Jia, Y., Zhao, Y., Gao, H., Kang, R., Wang, X., Tang, D., and Dai, E. (2019). Lipid storage and lipophagy regulates ferroptosis. Biochem. Biophys. Res. Commun. *508*, 997–1003.

Bersuker, K., Hendricks, J.M., Li, Z., Magtanong, L., Ford, B., Tang, P.H., Roberts, M.A., Tong, B., Maimone, T.J., Zoncu, R., et al. (2019). The CoQ oxidoreductase FSP1 acts parallel to GPX4 to inhibit ferroptosis. Nature *575*, 688–692.

Bogdan, A.R., Miyazawa, M., Hashimoto, K., and Tsuji, Y. (2016). Regulators of Iron Homeostasis: New Players in Metabolism, Cell Death, and Disease. Trends Biochem. Sci. *41*, 274–286.

Brovkovych, V., Aldrich, A., Li, N., Atilla-Gokcumen, G.E., and Frasor, J. (2019). Removal of Serum Lipids and Lipid-Derived Metabolites to Investigate Breast Cancer Cell Biology. Proteomics *19*, e1800370.

Butterfield, D.A., and Halliwell, B. (2019). Oxidative stress, dysfunctional glucose metabolism and Alzheimer disease. Nat. Rev. Neurosci. *20*, 148–160.

Chen, L., Chen, X.W., Huang, X., Song, B.L., Wang, Y., and Wang, Y. (2019). Regulation of glucose and lipid metabolism in health and disease. Sci. China Life Sci. *62*, 1420–1458.

Chen, X., Li, J., Kang, R., Klionsky, D.J., and Tang, D. (2020a). Ferroptosis: machinery and regulation. Autophagy, 1–28. https://doi.org/10.1080/15548627.2020.1810918.

Chen, X., Yu, C., Kang, R., and Tang, D. (2020b). Iron Metabolism in Ferroptosis. Front. Cell Dev. Biol. *8*, 590226.

Chen, X., Comish, P., Tang, D., and Kang, R. (2021a). Characteristics and biomarkers of ferroptosis. Front. Cell Dev. Biol. https://doi.org/10.3389/fcell.2021.637162.

Chen, X., Kang, R., Kroemer, G., and Tang, D. (2021b). Broadening horizons: the role of ferroptosis in cancer. Nat. Rev. Clin. Oncol. Published online January 29, 2021. https://doi.org/10.1038/s41571-020-00462-0.

Chen, X., Yu, C., Kang, R., Kroemer, G., and Tang, D. (2021c). Cellular degradation systems in ferroptosis. Cell Death Differ. https://doi.org/10.1038/s41418-020-00728-1.

Chu, B., Kon, N., Chen, D., Li, T., Liu, T., Jiang, L., Song, S., Tavana, O., and Gu, W. (2019). ALOX12 is required for p53-mediated tumour suppression through a distinct ferroptosis pathway. Nat. Cell Biol. *21*, 579–591.

Dai, E., Han, L., Liu, J., Xie, Y., Kroemer, G., Klionsky, D.J., Zeh, H.J., Kang, R., Wang, J., and Tang, D. (2020a). Autophagy-dependent ferroptosis drives tumor-associated macrophage polarization via release and uptake of oncogenic KRAS protein. Autophagy *16*, 2069–2083.

Dai, E., Han, L., Liu, J., Xie, Y., Zeh, H.J., Kang, R., Bai, L., and Tang, D. (2020b). Ferroptotic damage promotes pancreatic tumorigenesis through a TMEM173/STING-dependent DNA sensor pathway. Nat. Commun. *11*, 6339.

Dai, E., Meng, L., Kang, R., Wang, X., and Tang, D. (2020c). ESCRT-III-dependent membrane repair blocks ferroptosis. Biochem. Biophys. Res. Commun. *522*, 415–421.

Dai, E., Zhang, W., Cong, D., Kang, R., Wang, J., and Tang, D. (2020d). AIFM2 blocks ferroptosis independent of ubiquinol metabolism. Biochem. Biophys. Res. Commun. *523*, 966–971.

Dasgupta, B., and Seibel, W. (2018). Compound C/Dorsomorphin: Its Use and Misuse as an AMPK Inhibitor. Methods Mol. Biol. *1732*, 195–202.

Davì, G., Falco, A., and Patrono, C. (2005). Lipid peroxidation in diabetes mellitus. Antioxid. Redox Signal. *7*, 256–268.

DeBerardinis, R.J., and Chandel, N.S. (2016). Fundamentals of cancer metabolism. Sci. Adv. *2*, e1600200.

Deng, W., Zhu, S., Zeng, L., Liu, J., Kang, R., Yang, M., Cao, L., Wang, H., Billiar, T.R., Jiang, J., et al. (2018). The Circadian Clock Controls Immune Checkpoint Pathway in Sepsis. Cell Rep. *24*, 366–378.

Dixon, S.J., Lemberg, K.M., Lamprecht, M.R., Skouta, R., Zaitsev, E.M., Gleason, C.E., Patel, D.N., Bauer, A.J., Cantley, A.M., Yang, W.S., et al. (2012). Ferroptosis: an iron-dependent form of nonapoptotic cell death. Cell *149*, 1060–1072.

Dixon, S.J., Winter, G.E., Musavi, L.S., Lee, E.D., Snijder, B., Rebsamen, M., Superti-Furga, G., and Stockwell, B.R. (2015). Human Haploid Cell Genetics Reveals Roles for Lipid Metabolism Genes in Nonapoptotic Cell Death. ACS Chem. Biol. *10*, 1604–1609.

Doll, S., Proneth, B., Tyurina, Y.Y., Panzilius, E., Kobayashi, S., Ingold, I., Irmler, M., Beckers, J., Aichler, M., Walch, A., et al. (2017). ACSL4 dictates ferroptosis sensitivity by shaping cellular lipid composition. Nat. Chem. Biol. *13*, 91–98.

Doll, S., Freitas, F.P., Shah, R., Aldrovandi, M., da Silva, M.C., Ingold, I., Goya Grocin, A., Xavier da Silva, T.N., Panzilius, E., Scheel, C.H., et al. (2019). FSP1 is a glutathione-independent ferroptosis suppressor. Nature *575*, 693–698.

Dolma, S., Lessnick, S.L., Hahn, W.C., and Stockwell, B.R. (2003). Identification of genotype-selective antitumor agents using synthetic lethal chemical screening in engineered human tumor cells. Cancer Cell *3*, 285–296.

El Mjiyad, N., Caro-Maldonado, A., Ramírez-Peinado, S., and Muñoz-Pinedo, C. (2011). Sugar-free approaches to cancer cell killing. Oncogene *30*, 253–264.

Eling, N., Reuter, L., Hazin, J., Hamacher-Brady, A., and Brady, N.R. (2015). Identification of artesunate as a specific activator of ferroptosis in pancreatic cancer cells. Oncoscience *2*, 517–532.

Feng, H., and Stockwell, B.R. (2018). Unsolved mysteries: How does lipid peroxidation cause ferroptosis? PLoS Biol. *16*, e2006203.

Friedmann Angeli, J.P., Schneider, M., Proneth, B., Tyurina, Y.Y., Tyurin, V.A., Hammond, V.J., Herbach, N., Aichler, M., Walch, A., Eggenhofer, E., et al. (2014). Inactivation of the ferroptosis regulator Gpx4 triggers acute renal failure in mice. Nat. Cell Biol. *16*, 1180–1191.

Friedmann Angeli, J.P., Krysko, D.V., and Conrad, M. (2019). Ferroptosis at the crossroads of cancer-acquired drug resistance and immune evasion. Nat. Rev. Cancer *19*, 405–414.

Galluzzi, L., Vitale, I., Aaronson, S.A., Abrams, J.M., Adam, D., Agostinis, P., Alnemri, E.S., Altucci, L., Amelio, I., Andrews, D.W., et al. (2018). Molecular mechanisms of cell death: recommendations of the Nomenclature Committee on Cell Death 2018. Cell Death Differ. *25*, 486–541.

Gao, M., Monian, P., Quadri, N., Ramasamy, R., and Jiang, X. (2015). Glutaminolysis and Transferrin Regulate Ferroptosis. Mol. Cell *59*, 298–308.

Gao, M., Yi, J., Zhu, J., Minikes, A.M., Monian, P., Thompson, C.B., and Jiang, X. (2019). Role of Mitochondria in Ferroptosis. Mol. Cell *73*, 354–363.e3.

Gaschler, M.M., Andia, A.A., Liu, H., Csuka, J.M., Hurlocker, B., Vaiana, C.A., Heindel, D.W., Zuckerman, D.S., Bos, P.H., Reznik, E., et al. (2018). $FINO_2$ initiates ferroptosis through GPX4 inactivation and iron oxidation. Nat. Chem. Biol. *14*, 507–515.

Gout, P.W., Buckley, A.R., Simms, C.R., and Bruchovsky, N. (2001). Sulfasalazine, a potent suppressor of lymphoma growth by inhibition of the x(c)- cystine transporter: a new action for an old drug. Leukemia *15*, 1633–1640.

Grasso, C., Jansen, G., and Giovannetti, E. (2017). Drug resistance in pancreatic cancer: Impact of altered energy metabolism. Crit. Rev. Oncol. Hematol. *114*, 139–152.

Han, D., Jiang, L., Gu, X., Huang, S., Pang, J., Wu, Y., Yin, J., and Wang, J. (2020). SIRT3 deficiency is resistant to autophagy-dependent ferroptosis by inhibiting the AMPK/mTOR pathway and promoting GPX4 levels. J. Cell. Physiol. *235*, 8839–8851.

Hanahan, D., and Weinberg, R.A. (2011). Hallmarks of cancer: the next generation. Cell *144*, 646–674.

Hao, S., Liang, B., Huang, Q., Dong, S., Wu, Z., He, W., and Shi, M. (2018). Metabolic networks in ferroptosis. Oncol. Lett. *15*, 5405–5411.

Hassannia, B., Vandenabeele, P., and Vanden Berghe, T. (2019). Targeting Ferroptosis to Iron Out Cancer. Cancer Cell *35*, 830–849.

Hay, N. (2016). Reprogramming glucose metabolism in cancer: can it be exploited for cancer therapy? Nat. Rev. Cancer *16*, 635–649.

Hou, W., Xie, Y., Song, X., Sun, X., Lotze, M.T., Zeh, H.J., 3rd, Kang, R., and Tang, D. (2016). Autophagy promotes ferroptosis by degradation of ferritin. Autophagy *12*, 1425–1428.

Hsieh, M.C., Das, D., Sambandam, N., Zhang, M.Q., and Nahlé, Z. (2008). Regulation of the PDK4 isozyme by the Rb-E2F1 complex. J. Biol. Chem. *283*, 27410–27417.

Hu, N., Bai, L., Dai, E., Han, L., Kang, R., Li, H., and Tang, D. (2021). Pirin is a nuclear redox-sensitive modulator of autophagy-dependent ferroptosis. Biochem. Biophys. Res. Commun. *536*, 100–106.

Jeoung, N.H., Wu, P., Joshi, M.A., Jaskiewicz, J., Bock, C.B., Depaoli-Roach, A.A., and Harris, R.A. (2006). Role of pyruvate dehydrogenase kinase isoenzyme 4 (PDHK4) in glucose homoeostasis during starvation. Biochem. J. *397*, 417–425.

Jiang, L., Kon, N., Li, T., Wang, S.J., Su, T., Hibshoosh, H., Baer, R., and Gu, W. (2015). Ferroptosis as a p53-mediated activity during tumour suppression. Nature *520*, 57–62.

Jitrapakdee, S., St Maurice, M., Rayment, I., Cleland, W.W., Wallace, J.C., and Attwood, P.V. (2008). Structure, mechanism and regulation of pyruvate carboxylase. Biochem. J. *413*, 369–387.

Kagan, V.E., Mao, G., Qu, F., Angeli, J.P., Doll, S., Croix, C.S., Dar, H.H., Liu, B., Tyurin, V.A., Ritov, V.B., et al. (2017). Oxidized arachidonic and adrenic PEs navigate cells to ferroptosis. Nat. Chem. Biol. *13*, 81–90.

Kraft, V.A.N., Bezjian, C.T., Pfeiffer, S., Ringelstetter, L., Müller, C., Zandkarimi, F., Merl-Pham, J., Bao, X., Anastasov, N., Kössl, J., et al. (2020). GTP Cyclohydrolase 1/Tetrahydrobiopterin Counteract Ferroptosis through Lipid Remodeling. ACS Cent. Sci. *6*, 41–53.

Kuang, F., Liu, J., Tang, D., and Kang, R. (2020). Oxidative Damage and Antioxidant Defense in Ferroptosis. Front. Cell Dev. Biol. *8*, 586578.

Kuang, F., Liu, J., Xie, Y., Tang, D., and Kang, R. (2021). MGST1 is a redox-sensitive repressor of ferroptosis in pancreatic cancer cells. Cell Chem. Biol. *28*, 1–11.

Kwon, H.S., Huang, B., Unterman, T.G., and Harris, R.A. (2004). Protein kinase B-alpha inhibits human pyruvate dehydrogenase kinase-4 gene induction by dexamethasone through inactivation of FOXO transcription factors. Diabetes *53*, 899–910.

Leclerc, D., Pham, D.N., Lévesque, N., Truongcao, M., Foulkes, W.D., Sapienza, C., and Rozen, R. (2017). Oncogenic role of PDK4 in human colon cancer cells. Br. J. Cancer *116*, 930–936.

Lee, H., Zandkarimi, F., Zhang, Y., Meena, J.K., Kim, J., Zhuang, L., Tyagi, S., Ma, L., Westbrook, T.F., Steinberg, G.R., et al. (2020). Energy-stress-mediated AMPK activation inhibits ferroptosis. Nat. Cell Biol. *22*, 225–234.

Li, L., Kang, H., Zhang, Q., D'Agati, V.D., Al-Awqati, Q., and Lin, F. (2019a). FoxO3 activation in hypoxic tubules prevents chronic kidney disease. J. Clin. Invest. *129*, 2374–2389.

Li, Y., Lou, W., Raja, V., Denis, S., Yu, W., Schmidtke, M.W., Reynolds, C.A., Schlame, M., Houtkooper, R.H., and Greenberg, M.L. (2019b). Cardiolipin-induced activation of pyruvate dehydrogenase links mitochondrial lipid biosynthesis to TCA cycle function. J. Biol. Chem. *294*, 11568–11578.

Li, C., Zhang, Y., Liu, J., Kang, R., Klionsky, D.J., and Tang, D. (2020a). Mitochondrial DNA stress triggers autophagy-dependent ferroptotic death. Autophagy, 1–13. https://doi.org/10.1080/15548627.2020.1739447.

Li, J., Chen, X., Kang, R., Zeh, H., Klionsky, D.J., and Tang, D. (2020b). Regulation and function of autophagy in pancreatic cancer. Autophagy, 1–22. https://doi.org/10.1080/15548627.2020.1847462.

Li, J., Liu, J., Xu, Y., Wu, R., Chen, X., Song, X., Zeh, H., Kang, R., Klionsky, D.J., Wang, X., and Tang, D. (2021). Tumor heterogeneity in autophagy-dependent ferroptosis. Autophagy, 1–14. https://doi.org/10.1080/15548627.2021.1872241.

Liu, Z., Chen, X., Wang, Y., Peng, H., Wang, Y., Jing, Y., and Zhang, H. (2014). PDK4 protein promotes tumorigenesis through activation of cAMP-response element-binding protein (CREB)-Ras homolog enriched in brain (RHEB)-mTORC1 signaling cascade. J. Biol. Chem. *289*, 29739–29749.

Liu, J., Kuang, F., Kroemer, G., Klionsky, D.J., Kang, R., and Tang, D. (2020). Autophagy-Dependent Ferroptosis: Machinery and Regulation. Cell Chem. Biol. *27*, 420–435.

Liu, J., Song, X., Kuang, F., Zhang, Q., Xie, Y., Kang, R., Kroemer, G., and Tang, D. (2021). NUPR1 is a critical repressor of ferroptosis. Nat. Commun. *12*, 647.

Menendez, J.A., and Lupu, R. (2007). Fatty acid synthase and the lipogenic phenotype in cancer pathogenesis. Nat. Rev. Cancer *7*, 763–777.

Muñoz-Pinedo, C., Ruiz-Ruiz, C., Ruiz de Almodóvar, C., Palacios, C., and López-Rivas, A. (2003). Inhibition of glucose metabolism sensitizes tumor cells to death receptor-triggered apoptosis through enhancement of death-inducing signaling complex formation and apical procaspase-8 processing. J. Biol. Chem. *278*, 12759–12768.

Olson, K.A., Schell, J.C., and Rutter, J. (2016). Pyruvate and Metabolic Flexibility: Illuminating a Path Toward Selective Cancer Therapies. Trends Biochem. Sci. *41*, 219–230.

Pavlova, N.N., and Thompson, C.B. (2016). The Emerging Hallmarks of Cancer Metabolism. Cell Metab. *23*, 27–47.

Pettersen, I.K.N., Tusubira, D., Ashrafi, H., Dyrstad, S.E., Hansen, L., Liu, X.Z., Nilsson, L.I.H., Løvsletten, N.G., Berge, K., Wergedahl, H., et al. (2019). Upregulated PDK4 expression is a sensitive marker of increased fatty acid oxidation. Mitochondrion *49*, 97–110.

Röder, P.V., Wu, B., Liu, Y., and Han, W. (2016). Pancreatic regulation of glucose homeostasis. Exp. Mol. Med. *48*, e219.

Röhrig, F., and Schulze, A. (2016). The multifaceted roles of fatty acid synthesis in cancer. Nat. Rev. Cancer *16*, 732–749.

Saltiel, A.R., and Kahn, C.R. (2001). Insulin signalling and the regulation of glucose and lipid metabolism. Nature *414*, 799–806.

Saunier, E., Benelli, C., and Bortoli, S. (2016). The pyruvate dehydrogenase complex in cancer: An old metabolic gatekeeper regulated by new pathways and pharmacological agents. Int. J. Cancer *138*, 809–817.

Schott, C., Graab, U., Cuvelier, N., Hahn, H., and Fulda, S. (2015). Oncogenic RAS Mutants Confer Resistance of RMS13 Rhabdomyosarcoma Cells to Oxidative Stress-Induced Ferroptotic Cell Death. Front. Oncol. *5*, 131.

Scott, J.W., Galic, S., Graham, K.L., Foitzik, R., Ling, N.X., Dite, T.A., Issa, S.M., Langendorf, C.G., Weng, Q.P., Thomas, H.E., et al. (2015). Inhibition of AMP-Activated Protein Kinase at the Allosteric Drug-Binding Site Promotes Islet Insulin Release. Chem. Biol. *22*, 705–711.

Shintoku, R., Takigawa, Y., Yamada, K., Kubota, C., Yoshimoto, Y., Takeuchi, T., Koshiishi, I., and Torii, S. (2017). Lipoxygenase-mediated generation of lipid peroxides enhances ferroptosis induced by erastin and RSL3. Cancer Sci. *108*, 2187–2194.

Song, X., Zhu, S., Chen, P., Hou, W., Wen, Q., Liu, J., Xie, Y., Liu, J., Klionsky, D.J., Kroemer, G., et al. (2018a). AMPK-Mediated BECN1 Phosphorylation Promotes Ferroptosis by Directly Blocking System X_c^- Activity. Curr. Biol. *28*, 2388–2399.e5.

Song, X., Zhu, S., Xie, Y., Liu, J., Sun, L., Zeng, D., Wang, P., Ma, X., Kroemer, G., Bartlett, D.L., et al. (2018b). JTC801 Induces pH-dependent Death Specifically in Cancer Cells and Slows Growth of Tumors in Mice. Gastroenterology *154*, 1480–1493.

Soula, M., Weber, R.A., Zilka, O., Alwaseem, H., La, K., Yen, F., Molina, H., Garcia-Bermudez, J., Pratt, D.A., and Birsoy, K. (2020). Metabolic determinants of cancer cell sensitivity to canonical ferroptosis inducers. Nat. Chem. Biol. *16*, 1351–1360.

Sradhanjali, S., and Reddy, M.M. (2018). Inhibition of Pyruvate Dehydrogenase Kinase as a Therapeutic Strategy against Cancer. Curr. Top. Med. Chem. *18*, 444–453.

Stockwell, B.R., Friedmann Angeli, J.P., Bayir, H., Bush, A.I., Conrad, M., Dixon, S.J., Fulda, S., Gascón, S., Hatzios, S.K., Kagan, V.E., et al. (2017). Ferroptosis: A Regulated Cell Death Nexus Linking Metabolism, Redox Biology, and Disease. Cell *171*, 273–285.

Sun, X., Ou, Z., Chen, R., Niu, X., Chen, D., Kang, R., and Tang, D. (2016). Activation of the p62-Keap1-NRF2 pathway protects against ferroptosis in hepatocellular carcinoma cells. Hepatology *63*, 173–184.

Tang, D., and Kroemer, G. (2020). Ferroptosis. Curr. Biol. *30*, R1292–R1297.

Tang, D., Kang, R., Berghe, T.V., Vandenabeele, P., and Kroemer, G. (2019). The molecular machinery of regulated cell death. Cell Res. *29*, 347–364.

Tang, D., Chen, X., Kang, R., and Kroemer, G. (2020). Ferroptosis: Molecular Mechanisms and Health Implications. Cell Res. *31*, 107–125.

Tarangelo, A., Magtanong, L., Bieging-Rolett, K.T., Li, Y., Ye, J., Attardi, L.D., and Dixon, S.J. (2018). p53 Suppresses Metabolic Stress-Induced Ferroptosis in Cancer Cells. Cell Rep. *22*, 569–575.

Thorens, B., and Mueckler, M. (2010). Glucose transporters in the 21st Century. Am. J. Physiol. Endocrinol. Metab. *298*, E141–E145.

Vanden Berghe, T., Linkermann, A., Jouan-Lanhouet, S., Walczak, H., and Vandenabeele, P. (2014). Regulated necrosis: the expanding network of non-apoptotic cell death pathways. Nat. Rev. Mol. Cell Biol. *15*, 135–147.

Vander Heiden, M.G., Cantley, L.C., and Thompson, C.B. (2009). Understanding the Warburg effect: the metabolic requirements of cell proliferation. Science *324*, 1029–1033.

Wang, J., Qian, Y., and Gao, M. (2018). Overexpression of PDK4 is associated with cell proliferation, drug resistance and poor prognosis in ovarian cancer. Cancer Manag. Res. *11*, 251–262.

Wen, Q., Liu, J., Kang, R., Zhou, B., and Tang, D. (2019). The release and activity of HMGB1 in ferroptosis. Biochem. Biophys. Res. Commun. *510*, 278–283.

Wu, P., Sato, J., Zhao, Y., Jaskiewicz, J., Popov, K.M., and Harris, R.A. (1998). Starvation and diabetes increase the amount of pyruvate dehydrogenase kinase isoenzyme 4 in rat heart. Biochem. J. *329*, 197–201.

Wu, D., Peng, F., Zhang, B., Ingram, A.J., Kelly, D.J., Gilbert, R.E., Gao, B., and Krepinsky, J.C. (2009). PKC-beta1 mediates glucose-induced Akt activation and TGF-beta1 upregulation in mesangial cells. J. Am. Soc. Nephrol. *20*, 554–566.

Wu, J., Zhao, Y., Park, Y.K., Lee, J.Y., Gao, L., Zhao, J., and Wang, L. (2018). Loss of PDK4 switches the hepatic NF-κB/TNF pathway from pro-survival to pro-apoptosis. Hepatology *68*, 1111–1124.

Wu, J., Minikes, A.M., Gao, M., Bian, H., Li, Y., Stockwell, B.R., Chen, Z.N., and Jiang, X. (2019). Intercellular interaction dictates cancer cell ferroptosis via NF2-YAP signalling. Nature *572*, 402–406.

Xie, Y., Hou, W., Song, X., Yu, Y., Huang, J., Sun, X., Kang, R., and Tang, D. (2016a). Ferroptosis: process and function. Cell Death Differ. *23*, 369–379.

Xie, Y., Song, X., Sun, X., Huang, J., Zhong, M., Lotze, M.T., Zeh, H.J.R., Kang, R., and Tang, D. (2016b). Identification of baicalein as a ferroptosis inhibitor by natural product library screening. Biochem. Biophys. Res. Commun. *473*, 775–780.

Xie, Y., Zhu, S., Song, X., Sun, X., Fan, Y., Liu, J., Zhong, M., Yuan, H., Zhang, L., Billiar, T.R., et al. (2017a). The Tumor Suppressor p53 Limits Ferroptosis by Blocking DPP4 Activity. Cell Rep. *20*, 1692–1704.

Xie, Y., Zhu, S., Zhong, M., Yang, M., Sun, X., Liu, J., Kroemer, G., Lotze, M., Zeh, H.J., 3rd, Kang, R., and Tang, D. (2017b). Inhibition of Aurora Kinase A Induces Necroptosis in Pancreatic Carcinoma. Gastroenterology *153*, 1429–1443.e5.

Xie, Y., Kuang, F., Liu, J., Tang, D., and Kang, R. (2020). DUSP1 Blocks Autophagy-Dependent Ferroptosis in Pancreatic Cancer. J. Pancreatol. *3*, 154–160.

Yagoda, N., von Rechenberg, M., Zaganjor, E., Bauer, A.J., Yang, W.S., Fridman, D.J., Wolpaw, A.J., Smukste, I., Peltier, J.M., Boniface, J.J., et al. (2007). RAS-RAF-MEK-dependent oxidative cell death involving voltage-dependent anion channels. Nature *447*, 864–868.

Yamaguchi, S., Moseley, A.C., Almeda-Valdes, P., Stromsdorfer, K.L., Franczyk, M.P., Okunade, A.L., Patterson, B.W., Klein, S., and Yoshino, J. (2018). Diurnal Variation in PDK4 Expression Is Associated With Plasma Free Fatty Acid Availability in People. J. Clin. Endocrinol. Metab. *103*, 1068–1076.

Yang, W.S., SriRamaratnam, R., Welsch, M.E., Shimada, K., Skouta, R., Viswanathan, V.S., Cheah, J.H., Clemons, P.A., Shamji, A.F., Clish, C.B., et al. (2014). Regulation of ferroptotic cancer cell death by GPX4. Cell *156*, 317–331.

Yang, C., Wang, S., Ruan, H., Li, B., Cheng, Z., He, J., Zuo, Q., Yu, C., Wang, H., Lv, Y., et al. (2019). Downregulation of PDK4 Increases Lipogenesis and Associates with Poor Prognosis in Hepatocellular Carcinoma. J. Cancer *10*, 918–926.

Yu, Y., Xie, Y., Cao, L., Yang, L., Yang, M., Lotze, M.T., Zeh, H.J., Kang, R., and Tang, D. (2015). The ferroptosis inducer erastin enhances sensitivity of acute myeloid leukemia cells to chemotherapeutic agents. Mol. Cell. Oncol. *2*, e1054549.

Yuan, H., Li, X., Zhang, X., Kang, R., and Tang, D. (2016). Identification of ACSL4 as a biomarker and contributor of ferroptosis. Biochem. Biophys. Res. Commun. *478*, 1338–1343.

Zaal, E.A., and Berkers, C.R. (2018). The Influence of Metabolism on Drug Response in Cancer. Front. Oncol. *8*, 500.

Zhang, M., Zhao, Y., Li, Z., and Wang, C. (2018). Pyruvate dehydrogenase kinase 4 mediates lipogenesis and contributes to the pathogenesis of nonalcoholic steatohepatitis. Biochem. Biophys. Res. Commun. *495*, 582–586.

Zhang, Y., Tan, H., Daniels, J.D., Zandkarimi, F., Liu, H., Brown, L.M., Uchida, K., O'Connor, O.A., and Stockwell, B.R. (2019). Imidazole Ketone Erastin Induces Ferroptosis and Slows Tumor Growth in a Mouse Lymphoma Model. Cell Chem. Biol. *26*, 623–633.e9.

Zhao, Y., Li, M., Yao, X., Fei, Y., Lin, Z., Li, Z., Cai, K., Zhao, Y., and Luo, Z. (2020). HCAR1/MCT1 Regulates Tumor Ferroptosis through the Lactate-Mediated AMPK-SCD1 Activity and Its Therapeutic Implications. Cell Rep. *33*, 108487.

Zheng, J., and Conrad, M. (2020). The Metabolic Underpinnings of Ferroptosis. Cell Metab. *32*, 920–937.

Zhou, B., Liu, J., Kang, R., Klionsky, D.J., Kroemer, G., and Tang, D. (2020). Ferroptosis is a type of autophagy-dependent cell death. Semin. Cancer Biol. *66*, 89–100.

Zhu, S., Zhang, Q., Sun, X., Zeh, H.J., 3rd, Lotze, M.T., Kang, R., and Tang, D. (2017). HSPA5 Regulates Ferroptotic Cell Death in Cancer Cells. Cancer Res. *77*, 2064–2077.

STAR★METHODS

KEY RESOURCES TABLE

REAGENT OR RESOURCE	SOURCE	IDENTIFIER
Antibodies		
SLC2A1 (Rabbit mAb)	Cell Signaling Technology	Cat#12939, RRID:AB_2687899
ALOX5 (Rabbit mAb)	Cell Signaling Technology	Cat#3289, RRID:AB_2226946
FASN (Rabbit mAb)	Cell Signaling Technology	Cat#3180, RRID:AB_2100796
ACACA (Rabbit polyAb)	Cell Signaling Technology	Cat#4190, RRID:AB_10547752
ACTB (Mouse mAb)	Cell Signaling Technology	Cat#3700, RRID:AB_2242334
PDK4 (Rabbit polyAb)	Proteintech	Cat#12949-1-AP, RRID:AB_2161499
SLC2A3 (Mouse mAb)	Santa Cruz Biotechnology	Cat#sc-74497, RRID:AB_1124974
PDHA1 (Mouse mAb)	Thermo Fisher Scientific	Cat#45-6600, RRID:AB_2533825
PC (Rabbit polyAb)	NOVUS	Cat#NBP1-49536, RRID:AB_10011589
Anti-mouse IgG, HRP-linked antibody	Cell Signaling Technology	Cat#7076, RRID:AB_330924
Anti-rabbit IgG, HRP-linked antibody	Cell Signaling Technology	Cat#7074, RRID:AB_2099233
Chemicals, peptides, and recombinant proteins		
Arachidonic acid	Cayman Chemical	90010
Palmitic acid	Cayman Chemical	10006627
MT47-100	ProbeChem	PC-61181
Z-DEVD-FMK	Selleck Chemicals	S7312
Dorsomorphin	Selleck Chemicals	S7840
Dichloroacetate	Selleck Chemicals	S8615
Z-VAD-FMK	Selleck Chemicals	S7023
IKE	Selleck Chemicals	S8877
Erastin	Selleck Chemicals	S7242
RSL3	Selleck Chemicals	S8155
FIN56	Selleck Chemicals	S8254
Ferrostatin-1	Selleck Chemicals	S7243
Liproxstatin-1	Selleck Chemicals	S7699
STS	Selleck Chemicals	S1421
Glucose	Sigma-Aldrich	G7021
Pyruvate	Sigma-Aldrich	TMS-005-C
Lactate	Sigma-Aldrich	PHR1113
DMK	Sigma-Aldrich	349631
Glutamine	Sigma-Aldrich	59202C
Glutamate	Sigma-Aldrich	G1149
Baicalein	Sigma-Aldrich	196322
Citrate	Sigma-Aldrich	S4641
High-glucose DMEM	Thermo Fisher Scientific	11995073
No-glucose DMEM	Thermo Fisher Scientific	11966025
DMSO	Sigma-Aldrich	472301
Phosphate buffered saline	Thermo Fisher Scientific	AM9625
Cell lysis buffer	Cell Signaling Technology	9803
4%-12% Criterion XT Bis-Tris gel	Bio-Rad	3450124
XT MES running buffer	Bio-Rad	1610789
PVDF membranes	Bio-Rad	1620233
TBST	Cell Signaling Technology	9997S
SuperSignal West Pico Chemiluminescent Substrate	Thermo Fisher Scientific	34080

(*Continued on next page*)

Continued

REAGENT OR RESOURCE	SOURCE	IDENTIFIER
SuperSignal West Femto Maximum Sensitivity Substrate	Thermo Fisher Scientific	34095
ssoFast EvaGreen Supermix	Bio-Rad	172-5204
Lipofectamine 3000	Thermo Fisher Scientific	L3000-015
Critical commercial assays		
BCA assay kit	Thermo Fisher Scientific	23225
Cell counting kit-8 kit	Dojindo Laboratories	CK04
RNeasy plus mini kit	QIAGEN	74136
iScript cDNA synthesis kit	Bio-Rad	170-8891
Lactate Colorimetric Assay Kit	Sigma-Aldrich	MAK058
Pyruvate Assay Kit	Sigma-Aldrich	MAK071
PDH Activity Assay Kit	Sigma-Aldrich	MAK183
α-KG Assay Kit	Sigma-Aldrich	MAK054
Glucose Uptake-Glo Assay Kit	Promega	J1341
Fatty acid assay kit	Abcam	ab65341
Citrate assay kit	Abcam	ab83396
Glutathione assay kit	Sigma-Aldrich	CS0260
HMGB1 ELISA kit	Sino-Test Corporation	326054329
Caspase-3 activity kit	Cell Signaling Technology	5723
CycLex AMPK Kinase Assay Kit	MBL International Corporation	CY-1182
Lipid peroxidation (MDA) assay kit	Sigma-Aldrich	MAK085
Iron assay kit	Sigma-Aldrich	MAK025
Experimental models: cell lines		
MIAPaCa2	ATCC	CRL-1420
PANC1	ATCC	CCL-1469
KPC	Herbert J. Zeh (University of Texas Southwestern Medical Center)	N/A
Ampkα1/α$^{-/-}$ MEFs	Benoit Viollet (Université Paris Descartes)	N/A
Ampkα1/α$^{+/+}$ MEFs	Benoit Viollet (Université Paris Descartes)	N/A
Experimental models: organisms/strains		
C57BL6/J mice	Charles River	Cat#27
Oligonucleotides		
ALOX5-shRNA-1 (sequence: CCGGCCCGTGATATCCAGT TTGATACTCGAGTATCAAACTG GATATCACGGGTTTTTG)	Sigma-Aldrich	This paper
ALOX5-shRNA-2 (sequence: CCGCTCAAGATCAGCAACAC TATTTCTCGAGAAATAGTGTT GCTGATCTTGATTTTTTG)	Sigma-Aldrich	This paper
PDHA1-shRNA (sequence: CCGGGCTGGTAGCATCCCG TAATTTCTCGAGAAATTACG GGATGCTACCAGCTTTTT)	Sigma-Aldrich	This paper
FASN-shRNA (sequence: CCGGCATGGAGCGTATCTG TGAGAACTCGAGTTCTCACA GATACGCTCCATGTTTTT)	Sigma-Aldrich	This paper

(*Continued on next page*)

Continued

REAGENT OR RESOURCE	SOURCE	IDENTIFIER
ACACA-shRNA (sequence: CCGGTACAAGGGATACAGG TATTTACTCGAGTAAATACC TGTATCCCTTGTATTTTTG)	Sigma-Aldrich	This paper
PC-shRNA (sequence: CCGGATGGGCATCCGCCTG GATAATCTCGAGATTATCCA GGCGGATGCCCATTTTTTTG)	Sigma-Aldrich	This paper
PDK4-shRNA (sequence: CCGGCTTTGTCTTCTGAGTC TATAGCTCGAGCTATAGACT CAGAAGACAAAGTTTTTTG)	Sigma-Aldrich	This paper
Pdk4-shRNA (sequence: CCGGCCAGAATTAAACCTC ACACAACTCGAGTTGTGTG AGGTTTAATTCTGGTTTTT)	Sigma-Aldrich	This paper
AMPKα1-shRNA (sequence: CCGGGTTGCCTACCATCTCAT AATACTCGAGTATTATGAGAT GGTAGGCAACTTTTT)	Sigma-Aldrich	This paper
AMPKα2-shRNA (sequence: CCGGCCCACTGAAACGAGCAA CTATCTCGAGATAGTTGCTCG TTTCAGTGGGTTTTT)	Sigma-Aldrich	This paper
SLC2A1 siRNA	Horizon Discovery Ltd	LQ-007509-02-0005
SLC2A3 siRNA	Horizon Discovery Ltd	LQ-007516-02-0005
PDK1 siRNA	Horizon Discovery Ltd	LQ-005019-00-0005
PDK2 siRNA	Horizon Discovery Ltd	LQ-005020-00-0005
PDK3 siRNA	Horizon Discovery Ltd	LQ-005021-00-0005
PDK4 siRNA	Horizon Discovery Ltd	LQ-019425-00-0005
IDH1 siRNA	Horizon Discovery Ltd	LQ-008294-01-0005
IDH2 siRNA	Horizon Discovery Ltd	LQ-004013-01-0005
IDH3A siRNA	Horizon Discovery Ltd	LQ-008753-01-0005
IDH3B siRNA	Horizon Discovery Ltd	LQ-009596-01-0005
PCK1 siRNA	Horizon Discovery Ltd	LQ-006796-00-0005
PCK2 siRNA	Horizon Discovery Ltd	LQ-006797-00-0005
FlexiPlate siRNA library	QIAGEN	1027411
See Table S1 for primers used for qPCR	This paper	Table S1
Recombinant DNA		
Human PDK4 cDNA	OriGene Technologies Inc.	RC201656
Software and algorithms		
Image Lab software 6.0	Bio-Rad	https://www.bio-rad.com/en-us/product/image-lab-software?ID=KRE6P5E8Z
CFX Manager software 2.0	Bio-Rad	https://www.bio-rad.com/en-us/sku/1845000-cfx-manager-software?ID=1845000
GraphPad Prism 8.4.3	GraphPad	https://www.graphpad.com/scientific-software/prism/
LipidSearch Software 5.0	Thermo Fisher Scientific	https://www.thermofisher.com/order/catalog/product/IQLAAEGABSFAPCMBFK#/IQLAAEGABSFAPCMBFK

RESOURCE AVAILABILITY

Lead contact

Further information and requests for resources and reagents should be directed to and will be fulfilled by the lead contact, Daolin Tang (daolin.tang@utsouthwestern.edu).

Materials availability

All unique/stable reagents generated in this study are available from the lead contact with a completed Materials Transfer Agreement.

Data and code availability

This study did not generate any unique datasets or code.

EXPERIMENTAL MODEL AND SUBJECT DETAILS

Mice model

We conducted all animal care and experiments in accordance with the Association for Assessment and Accreditation of Laboratory Animal Care guidelines and with approval from our institutional animal care and use committee. At 6 weeks of age, male C57BL/6J mice received standard diet ("SCD") or high-fat diet ("HFD"; 5.24 kcal/g with 20% energy derived from protein, 60% from fat, and 20% from carbohydrate; Research Diets; D12492) for 12 weeks. Then the mouse PDAC cell line KPC (male) was implanted subcutaneously into the right abdomen of SCD and HFD mice. Once the tumors reached 60-80 mm^3 at day 7, tumor-bearing mice were treated with IKE (40 mg/kg, i.p., *once every other day*) or the ferroptosis inhibitor liproxstatin-1 (10 mg/kg, i.p., *once every other day*) or the PDK inhibitor dichloroacetate (DCA, 50 mg/kg, i.p., *once every other day*) under the corresponding diet. Tumors volumes were calculated using the formula length × $width^2$ × $\pi/6$. Mice were health checked daily throughout the experiment and kept on a regular 12 hr light and dark cycle with normal diet in a pathogen-free barrier facility.

Cell culture

The PANC1 (CRL-1469, male) and MIAPaCa2 (CRL-1420, male) cell lines were obtained from the American Type Culture Collection. PANC1 (K-Ras^{G12D};$p53^{R273H}$) and MIAPaCa2 (K-Ras^{G12C};$p53^{R248W}$) contained KRAS and TP53 mutations and were sensitive to ferroptosis (Eling et al., 2015; Xie et al., 2020; Zhu et al., 2017). The mouse PDAC cell line KPC was derived from tumors from KPC mice (*Pdx1-Cre;K-*$Ras^{G12D/+}$*;p53*$^{R172H/+}$) and was a gift obtained from Herbert J. Zeh III (University of Texas Southwestern Medical Center) (Xie et al., 2017b). *Ampk*α*1*/$\alpha^{-/-}$ MEFs (male) were a gift from Benoit Viollet (Université Paris Descartes). PHsPDAC cells (male) were generated from patients with PDAC who underwent surgery as previously described (Song et al., 2018b). These cells were cultured in high-glucose Dulbecco's Modified Eagle's Medium (DMEM; Thermo Fisher Scientific, 11995073; the complete formulation was available in the link below: https://www.thermofisher.com/us/en/home/technical-resources/media-formulation.9.html) supplemented with 10% heat-inactivated fetal bovine serum (Thermo Fisher Scientific, A3840001) and 1% penicillin and streptomycin (Thermo Fisher Scientific, 15070-063) at 37°C, 95% humidity, and 5% CO_2. No-glucose DMEM (Thermo Fisher Scientific, 11966025; the complete formulation was available in the link below: https://www.thermofisher.com/us/en/home/technical-resources/media-formulation.49.html) was used as a control in the study of anticancer activity of ferroptosis activators. In addition to glucose, other components, including amino acids (e.g., L-Glutamine [4 mM]), vitamins, inorganic salts, and serum, were the same between high-glucose and no-glucose DMEM. High-glucose and no-glucose DMEM didn't contain glutamate and fatty acid. Animal serum used in cell culture provides lipids to cells (Brovkovych et al., 2019). In some experiments, we added 1, 5, or 25 mM glucose to these commercially available glucose-free DMEM (Thermo Fisher Scientific, 11966025). Cell line identity was validated by short tandem repeat profiling, and routine mycoplasma testing was negative for contamination. Dimethyl sulfoxide (DMSO) was used to prepare the stock solution of drugs. The final concentration of DMSO in the drug working solution in the cells was < 0.01%. 0.01% DMSO was used as a vehicle control in all cell culture assays.

METHOD DETAILS

Cell viability and death assay

Cell viability was assayed by a CCK8 kit (Dojindo Laboratories, CK04). In brief, cells were seeded into 96-well plates and incubated with the indicated treatments. Subsequently, 100 μL fresh medium was added to cells containing 10 μL CCK-8 solutions and incubated for 2 h (37°C, 5% CO_2). Absorbance at 450 nm was measured using a microplate reader (Cytation 5 Cell Imaging Multi-Mode Reader). In addition, a Countess II FL Automated Cell Counter (Thermo Fisher Scientific) was used to assay the percentages of dead cells after cell staining with 0.4% trypan blue solution (Thermo Fisher Scientific, T10282) or 5 nM SYTOX Red Dead Cell Stain (Thermo Fisher Scientific, S34859).

RNAi and gene transfection

Human PDK4 cDNA (RC201656) was obtained from OriGene Technologies Inc. *ALOX5*-shRNA-1 (sequence: CCGGCCCGTGATATCCAGTTTGATACTCGAGTATCAAACTGGATATCACGGGTTTTTG), *ALOX5*-shRNA-2 (sequence: CCGCTCAAGATCAGCAA-

CACTATTTCTCGAGAAATAGTGTTGCTGATCTTGATTTTTTG), *PDHA1*-shRNA (sequence: CCGGGCTGGTAGCATCCCGTAATT TCTCGAGAAATTACGGGATGCTACCAGCTTTTT), *FASN*-shRNA (sequence: CCGGCATGGAGCGTATCTGTGAGAACTCGAGT TCTCACAGATACGCTCCATGTTTTT), *ACACA*-shRNA (sequence: CCGGTACAAGGGATACAGGTATTTACTCGAGTAAATACCTG-TATCCCTTGTATTTTTG), *PC*-shRNA (sequence: CCGGATGGGCATCCGCCTGGATAATCTCGAGATTATCCAGGCGGATGCC-CATTTTTTTG), *PDK4*-shRNA (sequence: CCGGCTTTGTCTTCTGAGTCTATAGCTCGAGCTATAGACTCAGAAGACAAAGTTTTTTG), *Pdk4*-shRNA (sequence: CCGGCCAGAATTAAACCTCACACAACTCGAGTTGTGTGAGGTTTAATTCTGGTTTTT), *AMPKα1*-shRNA (sequence: CCGGGTTGCCTACCATCTCATAATACTCGAGTATTATGAGATGGTAGGCAACTTTTT), and *AMPKα2*-shRNA (seq uence: CCGGCCCACTGAAACGAGCAACTATCTCGAGATAGTTGCTCGTTTCAGTGGGTTTTT) were obtained from Sigma-Aldrich. All pre-designed and validated siRNAs targeting *SLC2A1* (LQ-007509-02-0005), *SLC2A3* (LQ-007516-02-0005), *PDK1* (LQ-005019-00-0005), *PDK2* (LQ-005020-00-0005), *PDK3* (LQ-005021-00-0005), *PDK4* (LQ-019425-00-0005), *IDH1* (LQ-008294-01-0005), *IDH2* (LQ-004013-01-0005), *IDH3A* (LQ-008753-01-0005), *IDH3B* (LQ-009596-01-0005), *PCK1* (LQ-006796-00-0005), and *PCK2* (LQ-006797-00-0005) were obtained from Horizon Discovery Ltd. Transfection with shRNA, siRNA, or cDNA was performed with Lipofectamine 3000 (Invitrogen, L3000-015) according to the manufacturer's instructions.

RNAi screening

A FlexiPlate siRNA library targeting 87 glucose metabolism-associated genes in 96-well plates was obtained from QIAGEN (1027411). In brief, PANC1 cells were seeded (5000 cells/well) into plates overnight. Then the cells were transfected with siRNA in Lipofectamine 3000 at 5 nM for 48 h before erastin (10 μM) treatment for another 24 h in the presence or absence of 25 mM glucose. The cell viability was assayed in PANC1 cells following erastin treatment in high-glucose (D1) or no-glucose (D2) medium. The cell viability inhibition score was shown as D1/D2.

Q-PCR analysis

Total RNA was extracted and purified from cultured cells using the RNeasy Plus Mini Kit (QIAGEN, 74136) according to the manufacturer's instructions. The RNA was quantified by determining absorbance at 260 nm. One μg of total RNA from each sample was reverse-transcribed into cDNA using the iScript cDNA synthesis kit (Bio-Rad, 170-8891) in a volume of 20 μl; cDNA from cell samples was amplified. Quantitative real-time PCR was performed using ssoFast EvaGreen Supermix (Bio-Rad, 172-5204) on the C1000 Touch Thermocycler CFX96 Real-Time System (Bio-Rad) according to the manufacturer's protocol. Analysis was performed using Bio-Rad CFX Manager software 2.0 (Bio-Rad). The gene expression was calculated via the $2^{-\Delta\Delta Ct}$ method and normalized to *18SRNA*/*18srna* (Deng et al., 2018). The relative concentrations of mRNA were expressed in arbitrary units based on the untreated group, which was assigned a value of 1. The primers, which were synthesized and desalted from Sigma-Aldrich, are shown in Table S1.

Western blot

Cells were lysed in 1 × cell lysis buffer (Cell Signaling Technology, 9803) containing protease inhibitor (ROCHE, 11836153001) on ice for 10 min. After centrifugation at 14,000 x g for 15 min at 4°C, the supernatants were collected and quantified using BCA assay (Thermo Fisher Scientific, 23225). The 30 μg of each sample was resolved on 4%–12% Criterion XT Bis-Tris gels (Bio-Rad, 3450124) in XT MES running buffer (Bio-Rad, 1610789) and transferred to PVDF membranes (Bio-Rad, 1620233) using the Trans-Blot Turbo Transfer Pack and System (Bio-Rad). After blocking by TBST containing 5% skim milk for 1 h, the membrane was incubated overnight at 4°C with various primary antibodies (1:500-1:1000). After incubation with peroxidase-conjugated secondary antibodies (1:2000) for 1 h at room temperature, the signals were visualized using enhanced chemiluminescence (Thermo Fisher Scientific, 34095) and analyzed using the ChemiDoc Touch Imaging System (Bio-Rad).

Lactate assay

Lactate production was measured using a Lactate Colorimetric Assay Kit (Sigma-Aldrich, MAK058). Cells (2×10^6) were homogenized in lactate assay buffer and centrifuged at 13,000 × g for 10 min to remove insoluble materials. The supernatants were de-proteinized with a 10 kDa MWCO spin filter to remove other enzymes. Next, 50 μL of the supernatants was mixed with 50 μL of the reaction mix and the reaction was incubated for 30 min at room temperature. Lactate levels were measured at 450 nm using a microplate reader. The relative level of lactate in all groups was calculated and normalized to protein concentration. The control group was assigned a value of 1, and the treatment group was then calculated relative to the control group.

Pyruvate assay

Pyruvate production was measured using a Pyruvate Assay Kit (Sigma-Aldrich, MAK071). Cells (2×10^6) were homogenized in 4 volumes of pyruvate assay buffer and the samples were centrifuged at 13,000 × g for 10 min to remove insoluble materials to collect the supernatants. The supernatants were de-proteinized with a 10 kDa MWCO spin filter prior to addition to the reaction. Next, 50 μL of the supernatants was mixed with 50 μL of the master reaction mix and the reaction was incubated for 30 min at room temperature. Absorbance at 587 nm was measured using a microplate reader (Cytation 5 Cell Imaging Multi-Mode Reader). The relative level of pyruvate in all groups was calculated and normalized to protein concentration. The control group was assigned a value of 1, and the treatment group was then calculated relative to the control group.

PDH activity assay

PDH activity was measured using a PDH Activity Assay Kit (Sigma-Aldrich, MAK183). In the assay, PDH converted pyruvate into an intermediate, which reduced the developer to a colored product with strong absorbance at 450 nm. Briefly, cells (1×10^6) were homogenized in 100 μL of ice-cold PDH assay buffer for 10 min and the samples were centrifuged at 10,000 × g for 5 min to remove insoluble materials to collect the supernatants. Next, 50 μL of the supernatants was mixed with 50 μL of the reaction mix and the reaction was incubated at 37°C for 2-3 min. The samples were measured at 450 nm initially and then were measured at 450 nm every 5 min at 37°C before the most active sample was near to or exceeded the end of the linear range of the standard curve. The relative maximum PDH activity in all groups was calculated and normalized to protein concentration. The control group was assigned a value of 1, and the treatment group was then calculated relative to the control group.

α-KG assay

The level of α-KG was measured using an α-KG Assay Kit (Sigma-Aldrich, MAK054). Briefly, cells (2×10^6) were homogenized in 100 μL of ice cold a-KG Buffer and the samples were centrifuged at 13,000 × g for 10 min to remove insoluble materials to collect the supernatants. The supernatants were de-proteinized with a 10 kDa MWCO spin filter prior to addition to the reaction. Next, 50 μL of the supernatants was mixed with 50 μL of the reaction mix and the reaction was incubated at 37°C for 30 min. The α-KG concentration was determined by a coupled enzyme assay, which resulted in a colorimetric (570 nm) product. The relative level of α-KG in all groups was calculated and normalized to protein concentration. The control group was assigned a value of 1, and the treatment group was then calculated relative to the control group.

Glucose uptake assay

The level of glucose uptake was measured using a Glucose Uptake-Glo Assay Kit (Promega, J1341), which provided a homogeneous bioluminescent method for measuring glucose uptake in mammalian cells based on the detection of 2-deoxyglucose-6-phosphate (2DG6P). After treatment with ferroptosis activator, the cells were removed from medium and then washed with PBS. Next, 50 μL of 1 mM 2-deoxyglucose (2DG) was added to the cells, which were incubated for 10 min at room temperature. Then 25 μL of acid detergent solution (stop buffer) was added to lyse the cells and terminate the uptake; 25 μL of high-pH buffer solution (neutralization buffer) was then added to neutralize the acid. Finally, 100 μL of 2DG6P detection reagent was added to the sample wells and the reaction was incubated at room temperature for 1-2 h. A Cytation 5 Cell Imaging Multi-Mode Reader was used to assay the luminescence. The relative level of glucose uptake in all groups was calculated and normalized to protein concentration. The control group was assigned a value of 100%, and the treatment group was then calculated relative to the control group.

Lipid peroxidation assay

The relative MDA concentration in cell or tumor lysates was assessed using a Lipid Peroxidation (MDA) Assay Kit (Sigma-Aldrich, MAK085). Briefly, MDA in the sample reacted with thiobarbituric acid (TBA) to generate an MDA-TBA adduct. The MDA-TBA adduct can be easily quantified colorimetrically (OD = 532 nm). In addition, C11-BODIPY dye (Thermo Fisher Scientific, D3861) was used to detect lipid peroxidation in cells. Oxidation of the polyunsaturated butadienyl portion of the dye resulted in a shift of the fluorescence emission peak from ~590 nm to ~510 nm. The relative level of MDA and C11-BODIPY in all groups was calculated and normalized to protein concentration. The control group was assigned a value of 100%, and the treatment group was then calculated relative to the control group.

Iron assay

The relative Fe^{2+} concentration in cells was assessed using an Iron Assay Kit (Sigma-Aldrich, MAK025). Briefly, cells (2×10^6) were homogenized in 4-10 volumes of iron assay buffer and the samples were centrifuged at 16,000 × g for 10 min to remove insoluble materials to collect the supernatants. To measure ferrous iron, we added 50 μL samples to sample wells in a 96-well plate and brought the volume to 100 μL per well with 5 μL assay buffer. After incubation of the reaction at 37°C for 30 min, the absorbance at 593 nm was measured using a microplate reader. The relative level of Fe^{2+} in all groups was calculated and normalized to protein concentration. The control group was assigned a value of 100%, and the treatment group was then calculated relative to the control group.

GSH assay

The relative GSH concentration in cell lysates was assessed using a kit from Sigma-Aldrich (#CS0260) according to the manufacturer's instructions. The measurement of GSH used a kinetic assay in which catalytic amounts (nmoles) of GSH caused a continuous reduction of 5,5′-dithiobis (2-nitrobenzoic acid) to 5-thio-2-nitrobenzoic acid and the GSSG formed was recycled by GSH reductase and NADPH. The reaction rate was proportional to the concentration of GSH up to 2 mM. The yellow product (5-thio-2-nitrobenzoic acid) was measured spectrophotometrically at 412 nm using a microplate reader. The relative level of GSH in all groups was calculated and normalized to protein concentration. The control group was assigned a value of 100%, and the treatment group was then calculated relative to the control group.

Fatty acid assay

The relative fatty acid concentration in cell lysates was assessed using a kit from Abcam (ab65341). In the assay, fatty acids were converted to their CoA derivatives (coenzyme A), which were subsequently oxidized, leading to the formation of color. Briefly, after washed with cold PBS, cells (2×10^6) were homogenized in 200 μL chloroform/Triton X-100 (1% Triton X-100 in pure chloroform) on ice for 15 min and the samples were centrifuged at 16,000 × g for 10 min to collect organic phase (lower phase). The samples were air-dried at 50°C in a fume hood to remove chloroform and then were vacuum dried for 30 min to remove trace chloroform. The dried lipids were diluted in 200 μL of fatty acid assay buffer by vortexing extensively for 5 min. Then 2 μL of Acyl-CoA synthetase reagent was added to 50 μL sample wells and the reaction was incubated for 30 min at 37°C. Finally, 50 μL of reaction mix was added to sample wells. After incubation of the reaction at 37°C for 30 min, the absorbance at 570 nm was measured using a microplate reader. The relative level of fatty acid in all groups was calculated and normalized to protein concentration. The control group was assigned a value of 1, and the treatment group was then calculated relative to the control group.

Citrate assay

The relative level of citrate in cell lysates was assessed using a kit from Abcam (ab83396). Briefly, cells (2×10^6) were washed with cold PBS and resuspended in 100 μL of assay buffer. After homogenizing the cells quickly by pipetting up and down a few times, the samples were centrifuged at 16,000 × g for 5 min at 4°C. The collected supernatants were de-proteinized with a 10 kDa MWCO spin filter prior to addition to the reaction. Next, 50 μL of the supernatants was mixed with 50 μL of the reaction mix and the reaction was incubated for 30 min at room temperature. Absorbance at 570 nm was measured using a microplate reader (Cytation 5 Cell Imaging Multi-Mode Reader). The relative level of citrate in all groups was calculated and normalized to protein concentration. The control group was assigned a value of 1, and the treatment group was then calculated relative to the control group.

HMGB1 and caspase-3 assay

Plasma HMGB1 or caspase-3 activity in tissue was assayed using an ELISA kit from Sino-Test Corporation (326054329) or Cell Signaling Technology (5723) according to the manufacturer's protocol.

AMPK kinase assay

The kinase activity of AMPK was assayed using an CycLex AMPK Kinase Assay Kit from MBL International Corporation (CY-1182) according to the manufacturer's protocol.

LC-MS/MS method for lipid analysis

Reverse phase chromatography was selected for LC separation using CSH C18 column (1.7 μm, 2.1 mm × 100 mm, Waters). The lipid extracts were re-dissolved in 200 μL 90% isopropanol/acetonitrile, centrifuged at 14000 g for 15 min, finally 3 μL of sample was injected. Solvent A was acetonitrile–water (6:4, v/v) with 0.1% formic acid and 0.1 mM ammonium formate and solvent B was acetonitrile–isopropanol (1:9, v/v) with 0.1% formic acid and 0.1 mM ammonium formate. The initial mobile phase was 30% solvent B at a flow rate of 300 μL/min. It was held for 2 min, and then linearly increased to 100% solvent B in 23 min, followed by equilibrating at 5% solvent B for 10 min.

Mass spectra was acquired by Q-Exactive Plus in positive and negative mode, respectively. ESI parameters were optimized and preset for all measurements as follows: source temperature, 300°C; capillary temperature, 350°C; the ion spray voltage, 3000V; S-lens RF level, 50%; and the scan range of the instruments, m/z 200-1800. LipidSearch Software 5.0 (Thermo Fisher Scientific) was used to identify lipid species based on MS/MS data.

Pyruvate oxidation flux assay

Pyruvate oxidation was determined by measuring the release of $^{14}CO_2$ from [1-^{14}C] pyruvate as described previously (Li et al., 2019b). In short, the indicated cells were incubated with 100 μm [1-^{14}C] pyruvate (specific activity, 0.1 μCi/ml; Perkin Elmer Life Sciences) for 3 hours in Dulbecco's PBS buffer (8 mM sodium phosphate, 2 mM potassium phosphate, 0.14 M NaCl, 10 mM KCl, pH 7.4) in glass vials. A center well containing 2 M NaOH was placed to trap CO_2. After shaking at 37°C for 1 hour, the medium was acidified with 2.6 M perchloric acid to a final concentration of 0.4 M to stop the reaction. After 3 hours of trapping, $^{14}CO_2$ collected in the center well was measured by liquid scintillation. The pyruvate oxidation flux was determined by the amount of pyruvate that was oxidized to CO_2, and was normalized to the protein content.

QUANTIFICATION AND STATISTICAL ANALYSIS

Data are presented as mean ± SD except where otherwise indicated. GraphPad Prism 8.4.3 was used to collect and analyze data. A one-way or two-way analysis of variance (ANOVA) with Tukey's multiple comparisons test was used for comparison among the different groups. A *P value* of < 0.05 was considered statistically significant. We did not exclude samples or animals. No statistical methods were used to predetermine sample sizes, but our sample sizes are similar to those generally employed in the field.